

Interfering with HuR–RNA Interaction: Design, Synthesis and Biological Characterization of Tanshinone Mimics as Novel, Effective HuR Inhibitors

Leonardo Manzoni,^{†,○} Chiara Zucal,^{‡,○} Danilo Di Maio,^{§,○} Vito G. D’Agostino,[‡] Natthakan Thongon,[‡] Isabelle Bonomo,[‡] Preet Lal,[‡] Marco Miceli,^{||} Vanessa Baj,^{||} Marta Brambilla,^{||} Linda Cerofolini,^{⊥,#} Saioa Elezgarai,^{||} Emiliano Biasini,^{‡,||} Claudio Luchinat,[#] Ettore Novellino,[◆] Marco Fragai,^{⊥,#} Luciana Marinelli,^{*,◆} Alessandro Provenzani,^{*,‡} and Pierfausto Seneci^{*,||}

[†]Institute of Molecular Science and Technology (ISTM), CNR, Via Golgi 19, 20133 Milan, Italy

[‡]Centre for Integrative Biology (CIBIO), University of Trento, Via Sommarive 9, 38123 Povo, Trento, Italy

[§]Scuola Normale Superiore, Piazza dei Cavalieri 7, I-56126 Pisa, Italy

^{||}Chemistry Department, University of Milan, Via Golgi 19, 20133 Milan, Italy

[⊥]Consorzio Interuniversitario di Risonanze Magnetiche di Metallo Proteine (CIRMMP), Via L. Sacconi 6, 50019 Sesto Fiorentino, Florence, Italy

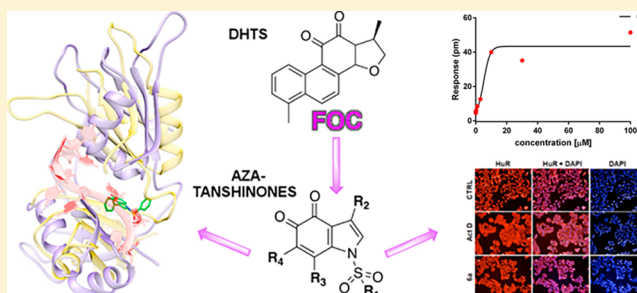
[#]CERM and Chemistry Department, University of Florence, Via della Lastruccia 3-13, 50019 Sesto Fiorentino, Florence, Italy

^{||}Istituto di Ricerche Farmacologiche Mario Negri, Milan, 20156, Italy

[◆]Pharmacy Department, University of Naples, Via Montesano 49, 80131 Naples, Italy

S Supporting Information

ABSTRACT: The human antigen R (HuR) is an RNA-binding protein known to modulate the expression of target mRNA coding for proteins involved in inflammation, tumorigenesis, and stress responses and is a valuable drug target. We previously found that dihydrotanshinone-I (DHTS, **1**) prevents the association of HuR with its RNA substrate, thus impairing its function. Herein, inspired by DHTS structure, we designed and synthesized an array of ortho-quinones (tanshinone mimics) using a function-oriented synthetic approach. Among others, compound **6a** and **6n** turned out to be more effective than **1**, showing a nanomolar K_i and disrupting HuR binding to RNA in cells. A combined approach of NMR titration and molecular dynamics (MD) simulations suggests that **6a** stabilizes HuR in a peculiar closed conformation, which is incompatible with RNA binding. Alpha screen and RNA-electrophoretic mobility shift assays (REMSA) data on newly synthesized compounds allowed, for the first time, the generation of structure activity relationships (SARs), thus providing a solid background for the generation of highly effective HuR disruptors.



■ INTRODUCTION

The human antigen R (HuR), also known as HuA or ELAVL1, is an ubiquitously expressed RNA binding protein that binds preferentially to adenine- and uridine-rich elements (ARE) of target coding and noncoding RNAs.^{1–3} HuR is primarily localized in the nucleus, where it exerts post-transcriptional functions such as splicing^{4,5} and alternative polyadenylation,⁶ although it shuttles to the cytoplasm carrying the targeted RNA to be spatiotemporally regulated in translation and stability.⁷ As a stress-response protein, HuR modulates the expression of target mRNA (containing AREs preferentially in their 3’UTR) coding for proteins involved in inflammation,⁸ cell division,⁹ tumorigenesis,^{10,11} angiogenesis,^{12,13} metastasis,¹⁴ senescence,¹⁵ apoptosis,^{16,17} immune,^{18,19} or stress responses.²⁰ The importance of HuR in inflammation and cancer has encouraged the research for

inhibitors/modulators to interfere with its biological activity.²¹ Several compounds have been named as HuR disruptors (i.e., molecules that can inhibit the HuR–RNA complex formation).^{22–30} For a detailed description of the known inhibitors and their properties, an exhaustive perspective has been recently published.³¹ However, neither systematic structure–activity relationships (SARs) studies, nor chemical synthesis of novel families of HuR inhibitors have been reported so far. From a structural point of view, rational design of HuR inhibitors is rather challenging due to the protein conformational plasticity.^{32–34} Moreover, HuR switches between at least two conformations upon binding/unbinding of its RNA substrate:

Received: August 12, 2017

Published: January 9, 2018

an “open” (apo) conformation, which is characterized by almost no contacts between its first two RNA recognition motif (RRM) domains, and a “closed” (holo) conformation, which is instead characterized by a few inter-residue contacts between the RRM domains.

Recently, as a result of a high throughput screening on a set of anti-inflammatory agents, we identified **1** (Dihydro-tanshinone-I, DHTS, Figure 1), a low-molecular-weight natural

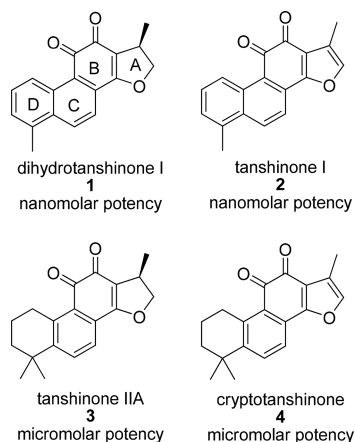


Figure 1. Naturally occurring tanshinones 1–4.

product able to interact with HuR, thus affecting its post-transcriptional functions.²⁷ Compound **1** is a major component of extracts from Danshen (*Salvia miltiorrhiza*) used in traditional Chinese medicine as a treatment for inflammation, cardiovascular, and cerebrovascular diseases.³⁵ Our detailed *in vitro* and *in vivo* characterization of **1** showed the HuR dependency of its mechanism of action²⁷ and its potency on cancer-linked HuR–mRNA interactions.¹¹ Naturally occurring tanshinones 2–4 (Figure 1) were tested as HuR inhibitors, observing a preference for an aryl condensed (compounds 1,2) vs saturated D rings (compounds 3,4).²⁷

Structural complexity has long hindered the synthetic exploitation of natural products as drug-oriented chemotypes. However, molecular editing through diverted total synthesis³⁶ and function-oriented synthesis (FOS)³⁷ are synthetic paths that help to transform a natural product to a simpler, equally active synthetic analogue.³⁸

We applied a FOS approach to **1**, starting from the bicyclic A–B scaffold **5** (Figure 2). It contains the *o*-quinone group

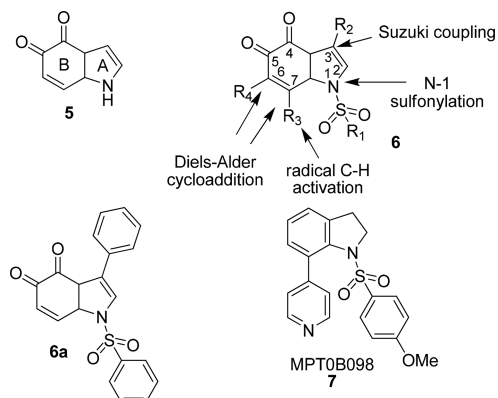


Figure 2. Tanshinone mimics as HuR inhibitors: core scaffold, function-oriented synthesis, active analogues.

and a pyrrole A ring, to provide novel, **1**-inspired, synthetic tanshinone mimics bearing R_1 – R_4 substitutions. Here the synthesis of a small library of tanshinone mimics **6a–t, w**, bearing substitutions in positions 1, 3, 6, and 7, is reported. Tanshinone mimics were tested for inhibition of HuR–RNA interactions and SARs were established. The most potent HuR inhibitor **6a** (Figure 2) was further characterized in a panel of *in vitro* and cellular assays and showed a direct K_D of 4.5 μ M to HuR. The molecular interaction of **6a** with HuR and with the HuR–mRNA complex was also elucidated via a combined approach of NMR and computational studies and grounded the path for the next generation of HuR inhibitors.

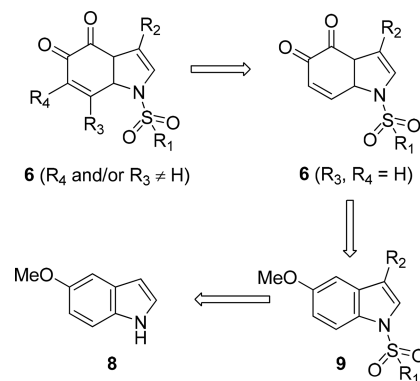
RESULTS AND DISCUSSION

Synthesis. Retrosynthesis. A FOS-based approach to natural products analogues entails the design of an uncomplicated synthetic strategy toward equally active, significantly simpler compounds. We built our strategy around a B ring-like ortho-quinone and we opted for a substituted, N-sulfonylated bicyclic A–B scaffold **6** as a function-oriented replacement for the tanshinone A–D ring system. The furan-pyrrole A ring switch was meant to provide HuR inhibition-inspired novelty, as the N-substituted indole MPT0B098 (**7**, Figure 2) is a negative modulator of HuR.³⁹ This compound bears a substituted sulfonamide in position 1, which was introduced on our A ring (scaffold **6**) to increase potency and further diversify our mimics from naturally occurring tanshinones.

We reasoned that a preliminary SAR around positions 1, 3, 6, and 7 on scaffold **6** could be established by exploiting N-sulfonylations (functionalization of N-1, $-\text{SO}_2\text{R}_1$), Suzuki couplings (functionalization of C-3, $-\text{R}_2$), radical CH functionalizations⁴⁰ and Michael additions (functionalization of C-7, $-\text{R}_3$) and Diels–Alder cycloadditions (functionalization of C-6 and C-7, $-\text{cycloR}_3\text{R}_4$, Figure 2).

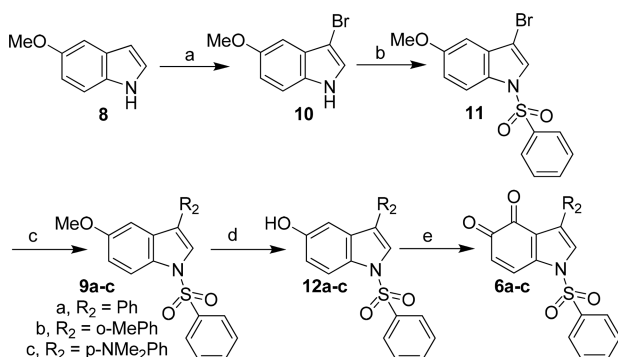
As to synthetic targets **6** ($R_1, R_2, R_4 \neq \text{H}$, or $R_1 - R_4 \neq \text{H}$, Scheme 1), we envisaged that functionalization of C-6 and/or

Scheme 1. Retrosynthetic Analysis to Tanshinone Mimics 6



C-7 could be carried out on 1,3-disubstituted indole-4,5-diones **6** ($R_3, R_4 = \text{H}$). Such compounds could be made by O-demethylation and oxidation of 1,3-disubstituted 5-methoxyindoles **9**. Compounds **9** could be prepared by 3-bromination of commercially available 5-methoxyindole **8**, followed by N-sulfonylation and Suzuki coupling (Scheme 1).

1-Alkyl/Arylsulfonyl-3-aryl Indole-4,5-Diones 6a–6j. The retrosynthetic scheme leading to 1,3-disubstituted indole-4,5-diones **6** ($R_1, R_2 \neq \text{H}$, $R_3 = R_4 = \text{H}$, Figure 1) was validated by synthesizing 1-phenylsulfonyl-3-phenyl indole-4,5-dione **6a** (Scheme 2). 5-Methoxyindole **8** was brominated in position

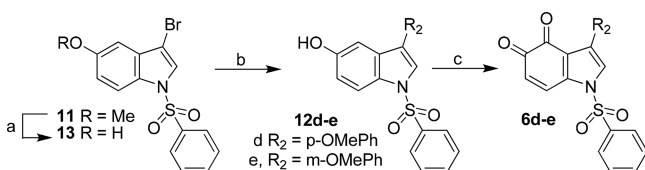
Scheme 2. Synthesis of 1-Phenylsulfonyl-3-aryl Indole-4,5-diones 6a–c^a

^aReagents and conditions: (a) Br₂, DMF, rt, 24 h, 74%; (b) PhSO₂Cl, *n*-Bu₄N⁺H₂SO₄⁻, aqueous 50% KOH, CH₂Cl₂, rt, 3 h, 90%; (c) arylboronic acid, Pd(PPh₃)₄, dry DME/EtOH 4/1, N₂ atmosphere, rt, reflux, 8 h, 83–92%; (d) 1 M BBr₃ in dry CH₂Cl₂, N₂ atmosphere, –78 to 5 °C, 87–99%; (e) IBX, EtOAc (40 °C) or DMF (rt), 2 to 24 h, 87–96%.

3 (step a, compound 10) and treated with phenylsulfonyl chloride (step b). 3-Bromo phenylsulfonamide 11 was reacted with phenyl boronic acid in a Suzuki coupling (step c) to provide, after careful optimization of the experimental protocol, 1-phenylsulfonyl-3-phenyl-5-methoxyindole 9a. Demethylation (step d, compound 12a) and oxidation with IBX⁴¹ (step e) led to 1-phenylsulfonyl-3-phenyl indole-4,5-dione 6a (Scheme 2) with an overall ≈35% yield.

3-Bromo phenylsulfonamide 11 was reacted with *o*- (R₂ = *o*-MePh, 9b) and *p*-substituted phenyl boronic acid (R₂ = *p*-NMe₂Ph, 9c) (step c), and respectively converted to 1-phenylsulfonyl-3-*o*-methylphenyl indole-4,5-dione 6b and 1-phenylsulfonyl-3-*p*-dimethylaminophenyl indole-4,5-dione 6c (steps d,e, Scheme 2) as reported for 6a.

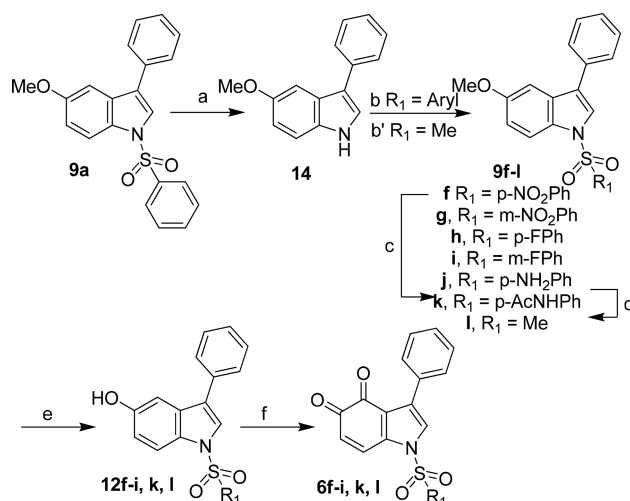
The synthesis of *p*-substituted (R₂ = *p*-OMe, 9d) and *m*-substituted (R₂ = *m*-OMe, 9e) aryl ethers (Scheme 3) required

Scheme 3. Synthesis of 1-Phenylsulfonyl-3-methoxyphenyl Indole-4,5-diones 6d,e^a

^aReagents and conditions: (a) 1 M BBr₃ in dry CH₂Cl₂, N₂ atmosphere, –78 to 5 °C, 86%; (b) methoxyphenylboronic acid, Pd(PPh₃)₄, dry DME/EtOH 4/1, N₂ atmosphere, rt, reflux, 8 h, 79–85%; (c) IBX, DMF, rt, 6 to 48 h, 67–87%.

demethylation of the 5-methoxy group on 3-bromo phenylsulfonamide 11 (step a) before Suzuki coupling (step b) and IBX oxidation (step c, Scheme 3) to avoid undesired demethylation of the 3-*m*- or *p*-methoxyphenyl group.

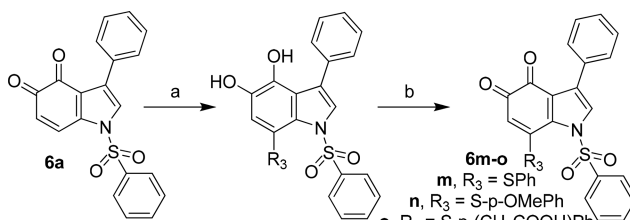
We attempted the synthesis of 1-alkylsulfonyl or 1-*m/p*-substituted arylsulfonyl-3-phenyl indole-4,5-diones 6f–l by replacing phenylsulfonyl chloride with alkyl- or *m/p*-arylsulfonyl chlorides (Scheme 2). Unfortunately, the Suzuki coupling protocol optimized for the synthesis of 9a was not applicable as such to other sulfonamides. Thus, we synthesized compounds 6f–i,k,l according to the longer, more efficient strategy depicted in Scheme 4.

Scheme 4. Synthesis of 1-Alkyl/Arylsulfonyl-3-phenyl Indole-4,5-diones 6f–i,k,l^a

^aReagents and conditions: (a) aqueous 3 M NaOH, 2/1 MeOH/THF, 80 °C, 2 h, 98%; (b) R₁SO₂Cl, *n*-Bu₄N⁺H₂SO₄⁻, 50% KOH, CH₂Cl₂, rt, 3 h, 87–92%; (b') NaH, mesyl chloride, dry DMF, N₂ atmosphere, 0 °C to rt, 3 h, 59%; (c) SnCl₂·2H₂O, 1/1 THF/MeOH, 80 °C, 2 h, 95%; (d) Ac₂O, pyridine, CH₂Cl₂, rt, 22 h, 82%; (e) 1 M BBr₃ in dry CH₂Cl₂, N₂ atmosphere, –78 to 5 °C, 73–99%; (f) IBX, EtOAc (40 °C) or DMF (rt), 2 to 24 h, 87–96%.

1-Phenylsulfonyl-3-phenyl-5-methoxyindole 9a was desulfonylated (step a, compound 14) and treated with aryl- (step b) or alkylsulfonamides (step b') to provide 1-*m/p*-substituted arylsulfonyl- and 1-methylsulfonyl-3-phenyl-5-methoxyindoles (respectively 9f–i and 9l) in good to excellent yields. 1-*p*-Nitrophenylsulfonyl-3-phenyl-5-methoxyindole 9f was reduced (step c, amine 9j) and acetylated to 1-*p*-acetamidophenylsulfonyl-3-phenyl-5-methoxyindole 9k (step d). Conversion of aryl ethers 9f–i,k,l into 1-*m/p*-substituted arylsulfonyl- or 1-alkylsulfonyl-3-phenyl indole-4,5-diones 6f–i,k,l (steps e and f, Scheme 4) was carried out as previously described for 6a.

1-Phenylsulfonyl-3-phenyl-7-thioaryl Indole-4,5-diones 6m–6o. The retrosynthetic scheme leading to 1,3,7-trisubstituted indole-4,5-diones 6 (R₁, R₂ ≠ H, R₃ = S–Ar, R₄ = H, Figure 2) was validated by synthesizing 1-phenylsulfonyl-3-phenyl-7-thiophenylindole-4,5-dione 6m (Scheme 5) via

Scheme 5. Synthesis of 1-Phenylsulfonyl-3-phenyl-7-thioaryl Indole-4,5-diones 6m–6o^a

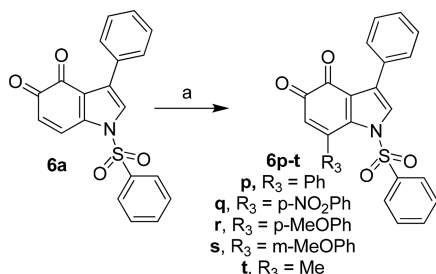
^aReagents and conditions: (a) aryl thiol, DMF, 2–3 h, rt, 62–88%; (b) IBX, DMF, 2 h, rt, 52–56%.

Michael addition of substituted benzenethiols on *o*-quinones.⁴¹ Namely, 1-phenylsulfonyl-3-phenyl indole-4,5-dione 6a was treated with thiophenol (step a), providing 1-phenylsulfonyl-3-phenyl-7-thiophenylindole-4,5-dione 6m after oxidation of the reduced form (step b, Scheme 5) in moderate yield after

extensive optimization. The optimized experimental protocol was used with *p*-methoxybenzenethiol (**6n**) and *p*-carboxymethylbenzenethiol (**6o**), observing moderate two step yields for both quinones.

1-Phenylsulfonyl-3-phenyl-7-aryl Indole-4,5-diones 6p–6t. The retrosynthetic scheme leading to 1,3,7-trisubstituted indole-4,5-diones (**6** ($R_1, R_2, R_3 \neq H, R_4 = H$, Figure 1) was validated by synthesizing 1-phenylsulfonyl-3,7-diphenylindole-4,5-dione **6p** (Scheme 6) via Mn(III)-mediated radical addition of boronic

Scheme 6. Synthesis of 1-Phenylsulfonyl-3-phenyl-7-aryl Indole-4,5-diones 6p–6t^a

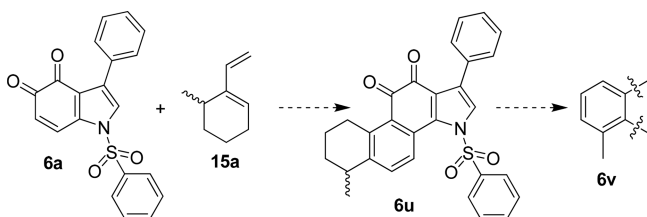


^aReagents and conditions: (a) boronic acid, Mn(OAc)₃, 1,2-dichloroethane, 80 °C, 30 to 150 min, 14–36%.

acids.^{40,42} 1-Phenylsulfonyl-3-phenyl indole-4,5-dione **6a** was treated with phenylboronic acid and Mn(OAc)₃ (step a), providing 1-phenylsulfonyl-3,7-diphenylindole-4,5-dione **6p** (Scheme 6). The experimental protocol required extensive optimization, and a moderate yield was finally obtained. The optimized experimental protocol was then used with aryl- (**6q–s**) and alkylboronic acids (**6t**), adapting the reaction time to each substrate (Scheme 5) and observing poor to moderate reaction yields.

Diels–Alder Cycloadducts 6u–6w. Validation of the retrosynthetic scheme to 1,3,6,7-tetrasubstituted indole-4,5-diones **6** ($R_1, R_2 \neq H$, cyclo R_3, R_4 , Figure 1) targeted 1-phenyl-3-phenylsulfonyl-6-methylphenanthro[1,2-*b*]pyrrole-10,11-dione **6v**. We envisaged a Diels–Alder cycloaddition between 1-phenylsulfonyl-3-phenyl indole-4,5-dione **6a** and 6-methyl-1-vinylcyclohexene **15a**, followed by DDQ dehydrogenation/aromatization of tetrahydrocycloadduct **6u** to aromatic **6v** (Scheme 7).⁴³ Unfortunately, we could not obtain pure diene

Scheme 7. Attempted Synthesis of 6,7,8,9-Tetrahydro-1-phenyl-3-phenylsulfonyl-phenanthro[1,2-*b*]indole-10,11-dione 6v



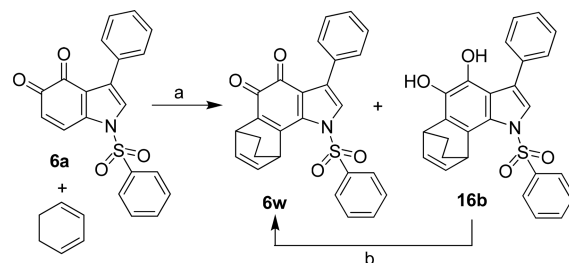
15a in reasonable amounts following the published synthetic procedure.⁴³

Due to the inhibitory activity observed with bicyclic indole-4,5-dione **6a** and some of its congeners, a tetracyclic, tanshinone-like core should not be necessarily needed to prevent HuR–mRNA interactions. Thus, cycloadditions on dienophile **6a** were targeted to introduce potency-oriented (additional interactions with the binding site on HuR) and/or

“druggability”-oriented substitutions on C-6 and C-7 (modulation of selectivity, solubility, and lipophilicity, etc.).

Diels–Alder cycloaddition between 1,3-cyclohexadiene **15b** and dienophile **6a** provided a mixture of desired *ortho*-quinone **6w** and diphenol **16b** (step a, Scheme 8). Oxidation (step b) converted the mixture to pure **6w**.

Scheme 8. Synthesis of Cycloadduct 6w^a



^aReagents and conditions: (a) cat. dry ZnCl₂, dry CH₂Cl₂, Ar atmosphere, 0 °C, 5 min, 88%; (b) CAN, 2/1 MeCN/H₂O, 0 °C, 10 min, quantitative.

A more systematic effort toward tanshinone-like 1,3,6,7-tetrasubstituted indole-4,5-diones **6** ($R_1, R_2 \neq H$, cyclo R_3, R_4 , Figure 1) will be carried out, and reported in future.

Biochemical Characterization. Compounds 6a and 6n Are More Effective than 1 in Inhibiting the HuR–RNA Complex Formation. Tanshinone mimics **6a–i**, **6k–t**, and **6w** were evaluated using a previously developed biochemical tool based on Amplified Luminescent Proximity Homogenous Assay AlphaScreen technology.^{27,28} Recombinant His-tagged HuR (rHuR) bound to nickel chelate acceptor beads was incubated with a biotinylated single-strand AU-rich RNA probe (Bi–AU), recognized by streptavidin-coated donor beads. When rHuR binds to the Bi–AU, the beads are brought into proximity and a fluorescent signal can be detected. We evaluated the ability of tanshinone mimics to inhibit the rHuR–Bi–AU complex formation in saturation binding conditions. Knowing that the K_D value for the rHuR–Bi–AU interaction is 2.5 nM,²⁷ we fitted on AlphaScreen saturation curves the K_i values, quantifying the inhibitory efficiency of tested compounds from high to low nanomolar range (Table 1). Among tanshinone mimics showing K_i with a percentage of inhibition >50%, compounds **6a** ($K_i = 12.8$ nM) and **6n** ($K_i = 15$ nM) were more effective than **1**, whereas compounds **6h**, **6k**, **6l**, **6r**, and **6s** showed similar activity (Figure 3 and Table 1). Consistently with previous data,²⁷ K_i value of our compounds changes according to the host in which the recombinant protein is produced (Supporting Figure 1).

Tanshinone mimics **6b**, **6f**, **6m**, and **6o** resulted interfered with the emitted fluorescence in AlphaScreen;^{44,45} thus, we proceeded with a second independent, orthogonal assay protocol for these and a few other tanshinone mimics (Figure 4 and Supporting Figures 2 and 3). We evaluated their inhibitory activity via a non denaturing and non-cross-linked REMSA.^{27,28} After we mixed at least 10-fold excess of rHuR with 75 fmol of 5′-DY681-labeled AU-rich RNA probe (DY681-AU) or with 25 nM of FAM-RNA probe, we observed the formation of the higher, oligomeric molecular weight complex between protein and RNA. The concomitant addition of active tanshinone mimics (5 μM concentration) caused a reduction of the shifted RNA probe, allowing qualitative estimation of their inhibitory ability toward the Bi–AU ligand at equilibrium. We noticed a

Table 1. Abilities of Tanshinone Mimics To Inhibit the rHuR–Bi–AU Complex Formation^a

Cpd	Structure	K _i , ¹ nM	Cpd	Structure	K _i , ¹ nM
1		50	6a		12.8
6b		Interfering*	6c		>100
6d		>200	6e		>200
6f		Interfering*	6g		>100
6h		48	6i		>100
6k		81	6l		56
6m		Interfering*	6n		15
6o		Interfering*	6p		>100
6q		>100	6r		41
6s		55	6t		>200
6w		>300			

^aNotes: ¹Concentration (nM) leading to half-maximal inhibition of rHuR–Bi–AU complex. *Interfering with the fluorescence spectra of excitation–emission of donor and acceptor beads (histidine (nickel) chelate detection kit).

concordance between the two biochemical assays for compounds **6a**, **6c**, **6k**, **6n**, **6p–6t**, and **6w**. Tanshinone mimics **6b**,

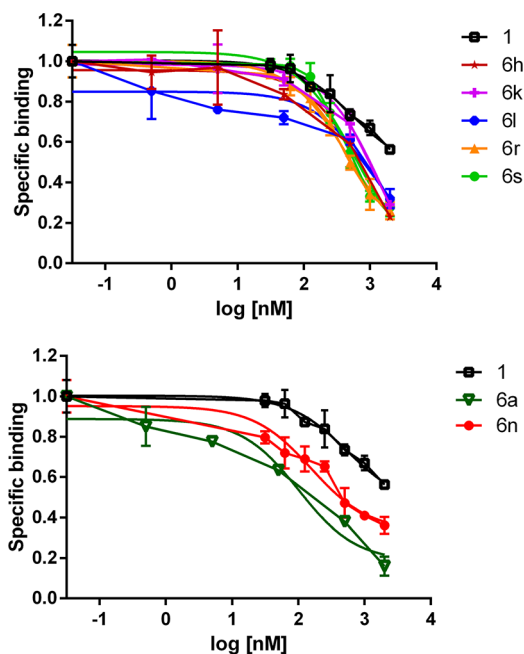


Figure 3. K_i calculation by Alpha screen assessing specific binding of His-tagged HuR and the AU-rich biotinylated RNA. K_i were calculated with respect to a K_D of 2.5 nM for the rHuR–Bi–AU interaction and normalized to control (DMSO). Fitting curves show nonlinear regression fits of the data according to a 1-site binding model in GraphPad Prism. Plotted bars are mean ± SD of two independent experiments.

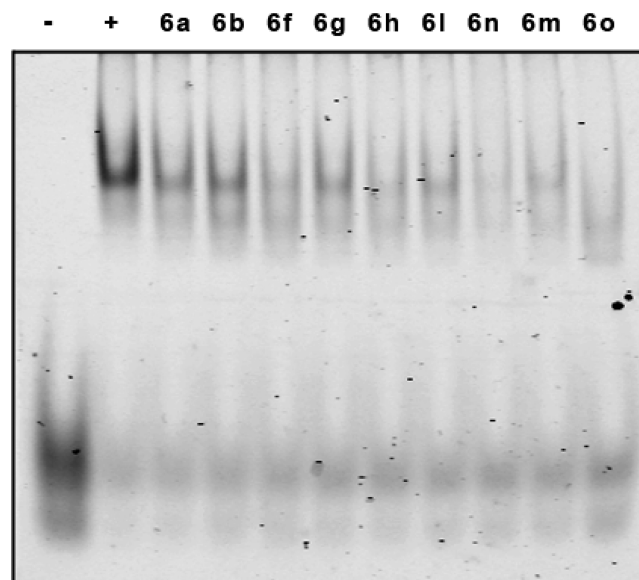


Figure 4. REMSA characterization of selected tanshinone mimics. REMSA assay performed with at least 10-fold excess of recombinant HuR incubated for 30 min with 75 fmol of 5'-DY681-labeled RNA probe. Incubation with RNA probe only (-), with rHuR, RNA probe and DMSO (+) used as positive control of the binding, and incubation with tanshinone mimics **6** (5 μM).

6f, **6m**, and **6o** were therefore classified as inhibitors endowed with intermediate potency (Figure 4). Compound **6a** was tested for binding to RNA probe via REMSA and circular dichroism (CD) (Supporting Figure 4A,B), showing no interference with the fluorescent probe and no change of the RNA conformation, thus suggesting the absence of an interaction with RNA.

Tanshinone Mimic 6a Directly Binds to HuR Protein and Modulates Its Binding with Intracellular Target mRNAs. Compound 6a was selected among the most potent tanshinone mimics for further evaluation. It showed a similar mechanism to 1 in interacting with the truncated form of HuR comprising the first two RRM domains (RRM1-RRM2) but not with the third domain (RRM3) and not with the RNA probe (Supporting Figure 4 and 5).

Dynamic mass redistribution (DMR) analysis⁴⁶ revealed, in a label-free format, a direct protein:6a interaction at the equilibrium (Figure 5). Full-length rHuR was immobilized onto the

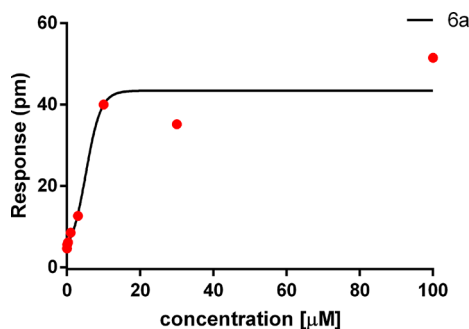


Figure 5. Compound 6a binds to recombinant HuR. Different concentrations of 6a were added to label-free microplate wells on which aliquots of full-length protein had previously been immobilized. Measurements were performed before (baseline, protein-coated wells) and after (final) adding the compound. The response (pm) was obtained subtracting the baseline output from the final output signals. The output signal for each well was obtained by subtracting the signal of the protein-coated reference area from the signal of uncoated area. The data (red dots) were fitted (black line) to a sigmoidal function using a 4-parameter logistic (4PL) nonlinear regression model: $R^2 = 0.944$; $p = 0.009$.

surface of label-free microplates by amine-coupling chemistry. Different amounts of 6a (0.03–100 μM) were added to the wells and the mass of molecular complexes was detected after 30 min incubation. Dose-dependent binding of 6a to rHuR was observed in the 0.3–10 μM range, sufficient to obtain saturation. The estimated affinity constant (K_D) was $\approx 4.5 \mu\text{M}$. The same experiment was performed with 1, but it was impossible to evaluate the K_D due to its poor solubility.²⁷

We then determined if 6a was interfering on HuR–RNA binding in MCF7 cells. We performed an RNA immunoprecipitation (RIP) assay⁴⁷ on MCF7 extracts testing three validated HuR transcripts. We clearly observed a subsequent decrease of the relative number of mRNA copies and a decreased expression level of such mRNAs (*ERBB2*, *CTNNB1*, *VEGF*) but not of non target genes (*RPLP0*, *HPRT1*) (Figure 6A,B). Therefore, compound 6a directly binds to HuR both *in vitro* and in cellular context, in a region contained between the first two RRM domains.

NMR and Molecular Modeling. *Tanshinone Mimic 6a Blocks HuR in a “Closed” Conformation.* The 2D ^1H – ^{15}N HSQC spectrum of RRM1-RRM2 domains showed well-dispersed signals in accordance with a folded protein structure, whose residues, including those of the linker region, have been previously assigned.²⁹ The resonances of residues forming the RRM1 domain are almost the same in the isolated domain⁴⁸ and in the RRM1-RRM2 construct. The large superimposition of the signals in the isolated RRM1 and in the tandem domains is in agreement with the relaxation data that show as the two domains move independently in solution in the absence of

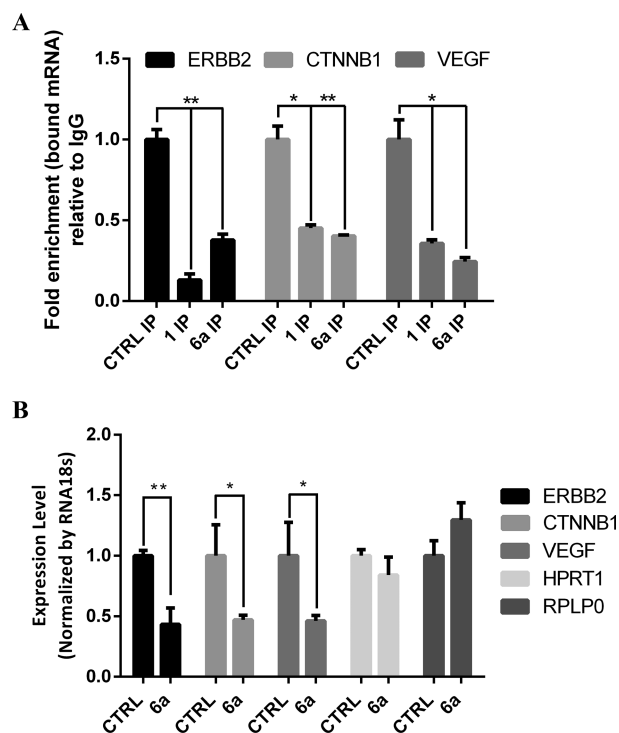


Figure 6. RIP and quantitative real-time PCR (qRT-PCR). (A) RIP was performed in MCF7 cells, lysed after 6 h treatment with DMSO (CTRL), 1 (1 μM) or 6a (5 μM). HuR antibody (IP) and an IgG isotype (IgG) were used for RNA precipitation. Changes in the mRNAs bound to HuR in the control or treatment condition were assessed by qRT-PCR and compared with the ones obtained with IgG precipitation, used as negative control. The relative values (Fold enrichment) were normalized to IgG, considering the value of the housekeeping gene *RPLP0*. (B) MCF7 were treated with 6a (5 μM) for 6 h to evaluate changes in total RNA levels. Expression level of *ERBB2*, *CTNNB1*, *VEGF*, *RPLP0*, and *HPRT1* were measured by qRT-PCR and normalized to *RNA18s*. Data are presented as mean \pm SD of a biological triplicate ($*p < 0.05$ and $**p < 0.01$ versus CTRL).

RNA.²⁹ In line with the previously reported crystal structures of HuR, each domain in the RRM1-RRM2 construct is constituted by two α -helices and four β -strands.⁴⁹

The molecular interaction of 6a with RRM1-RRM2 tandem domains of HuR was evaluated through solution NMR.⁵⁰ Compound 6a shows improved solubility with respect to 1.²⁹ Its effects on the protein are appreciable in the 2D ^1H – ^{15}N HSQC in the presence of 0.6 equiv of the ligand, whereas with 1 comparable effects were observed after the addition of 4 equiv. As also reported for 1,²⁹ a generalized decrease in signal intensity was observed for the protein resonances, with few residues (Thr20, Leu22, Val66, Ser94, Tyr95, Ile103, Asn107, Leu108, Tyr109, Ile133, Val137, Leu138, Val139, Ser146) experiencing a stronger effect (Figure 7). Tanshinone mimic 6a and 1 interact with the protein in the same region, i.e. the β -platform of both domains. In particular, eight amino acids (Thr20, Ser94, Tyr95, Asn107, Leu108, Ile133, Val137, Leu138) experience a decrease in signal intensity with both ligands.

The generalized decrease of signal intensity, together with the distribution of affected residues over the large surfaces of the β -platform in each domain suggests an alteration of the equilibrium between “closed” and “open” conformations upon ligand binding. Specifically, the decrease of signal intensity was consistent with a mechanism where compound 6a stabilizes a “closed” conformation of HuR. Collectively, NMR analysis

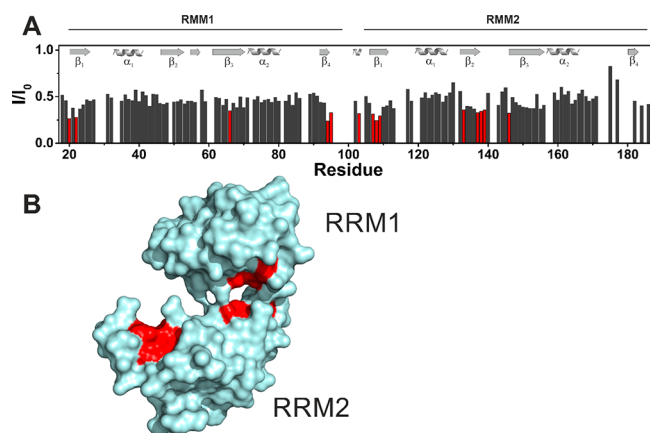


Figure 7. Compound **6a** stabilized recombinant HuR in a “closed” conformation. (A) Graphical representation of the intensity changes of RRM1-RRM2 HuR protein *per* residues in the presence of 0.6 equiv of **6a**. The residues exhibiting the highest decreases in signal intensities are colored in red. The secondary structures of the domains are reported on the graph. (B) Surface representation of the closed (PDB ID: 4ED5) conformation of HuR. The residues exhibiting the largest decrease in signal intensities in the presence of 0.6 equiv of **6a** are shown in red.

indicates that **1** and **6a** bind the HuR protein approximately in the same region, producing similar effects on protein dynamics. However, it is interesting to note that one residue (Ile103) of the interdomain linker (hereafter referred to as “hinge” loop) is

sensitive to **6a** and not to **1**. This experimental evidence would suggest for **6a** a binding site in a more close proximity of the hinge loop, with respect to **1**. To better explore this possibility, a molecular modeling study was performed.

To this purpose, a combined approach of docking calculations and extended molecular dynamics (MD) simulations was applied. Specifically, we first attempted a “blind” docking to the entire HuR surface, using two different docking software to better sample the binding space (AutoDock4.2 and Glide 6.5). Most of the highest-score poses of **6a** suggested by AutoDock were located within the RNA binding cleft (residues 18 to 95 of RRM1 and 107 to 185 of RRM2) and in proximity of the “hinge” loop. On the other hand, docking results with Glide converged toward one solution, which was different from those predicted by Autodock, though it was placed in proximity of the “hinge” loop as well. Therefore, albeit these results seem to indicate the region surrounding the “hinge” loop as the most likely binding region for **6a**, docking failed to unequivocally pinpoint one privileged binding mode, likely owing to omission of full receptor flexibility from the state-of-the-art docking software. To account for the missing receptor flexibility, we carried out multiple extended MD simulations on a reasonable number of **6a** binding modes, for a total simulation time of 6 μ s, and assessed their relative stability. Specifically, we opted for the binding pose predicted by Glide (Figure 8A) and the three best ranked and most diverse poses (in terms of root-mean-square deviation (RMSD) predicted by AutoDock) (Figure 8B,C,D). In all four cases, **6a** drifted away from its starting docking position and explored a significant portion of the HuR surface,

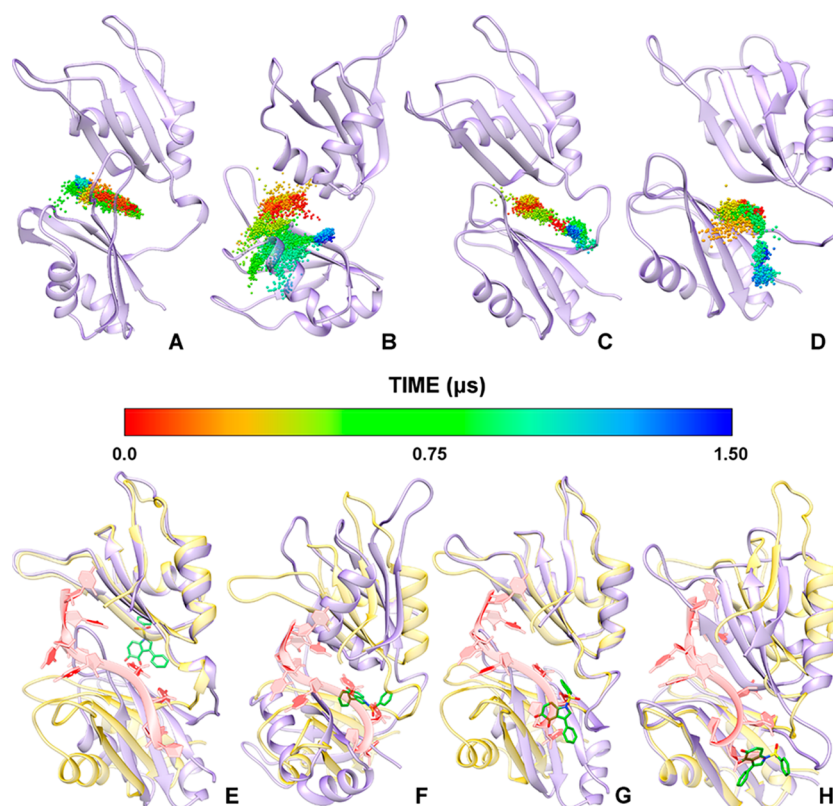


Figure 8. (A–D) **6a** exploration of the HuR RNA-binding pocket for each simulated pose. HuR is shown as purple cartoons, while the **6a** center of mass is shown as spheres colored according to the simulation time. (E,F) Global view of the HuR–**6a** complexes in each final MD simulation pose. Note how the binding of **6a** (green sticks) to HuR and the further closure of the mRNA binding cleft, as compared to the mRNA-bound conformation (yellow), prevent the accommodation of the mRNA strand (red ribbons). In both groups of pictures, panels related to the pose predicted by Glide and the three highest score poses predicted by Autodock are arranged from left to right, respectively.

as can be observed by following the movement of the center of mass of **6a** (Figure 8A–D), its RMSD vs time (Supporting Figure 6A) or its distance from the center of mass of the two RRM domains (Supporting Figure 6B). After about 1 μ s, each starting docking pose got stabilized and evolved to different final binding modes (Figure 8E–H) which remain individually stable for almost 500 ns. Specifically, out of the four final binding poses, one was located outside the RNA binding cleft (the Glide predicted binding pose, Figure 8E) while the other three were located within the latter pocket, in correspondence or in close proximity of the “hinge” loop. In these final poses **6a** stabilizes HuR in a conformational state that is structurally incompatible with RNA binding. In fact, in each case the two RRM domains were found to be more in contact with each other than in the HuR–RNA complex crystal structure (Figure 8E–H). Accordingly, we observed an increase in both the number of non-native interdomain contacts and the amount of surface area “buried” between the two RRM domains (see respectively Supporting Figure 7A and 7B). These results indicate that binding of **6a** to HuR is correlated with a closure of the RNA binding cleft and, consequently, with an overall decrease in the amount of interdomain space accessible for RNA binding.

Nevertheless, among the four poses issuing from our modeling approach, the one depicted in Figure 8F and more in detail in Figure 9 seems to be more in agreement with both the NMR

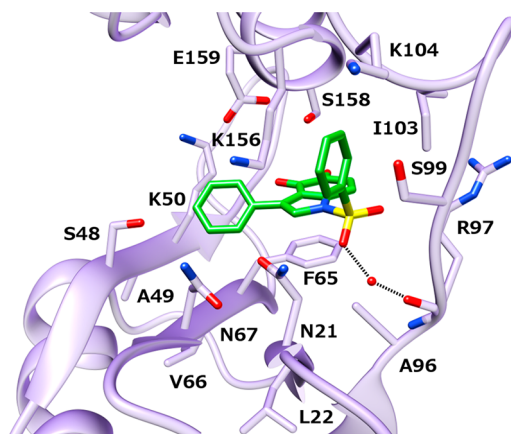


Figure 9. Most likely binding mode of **6a** (green sticks) to HuR (purple cartoons), as issuing from a representative structure of the last 500 ns of the MD simulation. HuR residues involved in binding interactions with **6a** are displayed as sticks.

data and the SARs reported here. Specifically, **6a** was found between the RRM1 beta sheets (β_1 , β_2 , β_3), the N-terminal part of the RRM2 α_2 helix and the “hinge” loop. In this binding arrangement (Figure 9), the phenyl ring in R_1 is accommodated in a narrow, laterally open, hydrophobic pocket, shaped by Ile103, Ser99, Lys104 and Lys156 residues, with which it establishes several CH- π interactions. Notably, one sulfonyloxygens establishes a water-bridged H-bond with the backbone C=O of Ala96, while the phenyl ring in R_2 , forms a cation- π interaction with Lys156 and several CH- π interactions with the CH₂ groups of Ser48, Lys50, Asn67 and Lys156. The indole-4, 5-dione moiety is inserted in a solvent exposed pocket, where it establishes CH- π interactions with Ala96, Lys156, Ser158 and, a π -stacking interaction with Phe65. In this regard, the quinone-oxygens, which point to the solvent exposed part of the pocket, likely play a crucial role in strengthening the π -stacking interaction with Phe65.

As compared to the other poses, in the above-described binding mode, **6a** is in close proximity with a larger number of HuR residues exhibiting the highest decreases in NMR signal intensity (Figure 7A). Precisely, these residues are Leu22, Val66, and Ile103. Notably, NMR pinpointed I103 in the “hinge” loop as a residue sensitive to binding of **6a** but not of **1**, which is known to stabilize HuR in a closed form without stably interacting with the “hinge” loop.²⁹ As compared to the other binding poses, which are located either outside the RNA binding cleft or in more solvent exposed regions, this binding mode (Figure 9) would be in line also with SARs studies. It would explain why substitutions on the phenyl ring in R_1 (**6f**, **6g**, **6h**, **6i**, **6k**, **6l**), though still causing a drop in the activity, are generally better tolerated than those on the phenyl ring in R_2 (**6b**, **6c**, **6d**, **6e**). In fact, thanks to the additional lateral space in the pocket hosting the phenyl ring in R_1 , this ring could slightly rotate around the S–N bond so as to allow the attachment of various substituents, even large ones as in the case of **6k**. This would not be possible at position R_2 , owing to potential steric clashes with residues shaping the pocket where it is hosted. This binding mode would also explain why the addition of electron-drawing substituents on the phenyl group in R_1 (**6f**, **6g**, **6h**, **6i**), particularly at the meta position (**6g**, **6i**), also causes a drop in the activity. In fact, these substitutions would likely weaken the aforementioned water-bridged H-bond with Arg97. Finally, SARs indicate that the addition of rigid and bulky substituents at position 6–7 (see **6w**) or 7 (**6p**, **6q**, **6r**, **6s**, **6t**) of the bicyclic scaffold (B ring) is also generally detrimental to binding. Steric clashes with the adjacent sulfonamidic group are very likely to arise as a result of their introduction, which would force a rotation around the S–N bond. That, according to our model, would in turn lead to a rupture of the water-bridged H-bond with Ala96 and of the hydrophobic interactions of the phenyl ring in R_1 . In the case of **6q**, but especially of **6r** and **6s**, the presence of a H-bond donor at position 7 may partially compensate for these detrimental effects through the potential formation of a H-bond with the near Arg97 side chain. The only exception to this trend is represented by **6n**, where the presence of a sulfur atom directly linked to the scaffold likely increases the rotational flexibility and makes the addition of a bulky group well tolerated.

In conclusion, our NMR and molecular modeling data provide useful insights into the binding mode and mechanism of action of this family of compounds, suggesting that they most likely bind HuR at the “hinge” region between the two RRM domains and stabilize HuR in a peculiar closed conformation, which is incompatible with RNA binding.

Biological Activity in Cancer Cell Lines. Selected Tanshinone Mimics Show Micromolar Cytotoxicity in Cancer Cells. We previously reported that the anticancer effects of **1** are influenced by HuR dosage, demonstrating that HuR is functionally connected with the intracellular effects of this pleiotropic natural product.²⁹ Similarly to **1**, the localization of HuR did not change during treatment with **6a** or other tanshinone mimics, suggesting that inhibition of HuR is connected with its binding performances and not with its subcellular localization (Figure 10).

We evaluated the cytotoxic effects of tanshinone mimics. Compounds **6a** and **6n** affected the viability of cells when treated for 72 h, together with **6b**, **6m**, **6k**, **6l** and **6t** at higher dosages (Figure 11). They were tested on breast cancer cell lines MCF7 and MDA-MB-231, and on pancreatic ductal adenocarcinoma cell line PANC-1. Tanshinone mimics were generally less effective

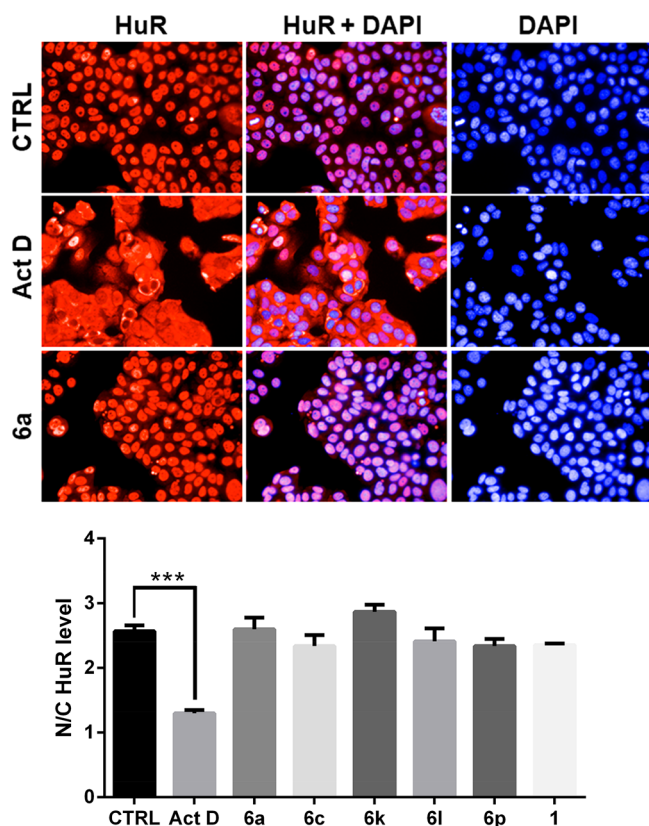


Figure 10. Representative immunofluorescence showing unchanged subcellular localization of HuR after **6a** treatment. HuR (red) or nuclei (blue, DAPI) after staining in MCF7 cells treated for 3 h with DMSO (CTRL) or 2.5 μM of actinomycin D (ActD)¹⁹ or 10 μM **6a**. Plotted in the graph are the ratio of HuR fluorescent signal between nucleus and cytoplasm (N/C). The image plate reader Operetta was used for image acquisition (40 \times high NA objective) and evaluation by selecting 13 fields/well. The ratio N/C represents the mean \pm SD of single cells for every well (***) $p < 0.001$.

tive than **1** on cell viability (Figure 11, Supporting Table S1), with an IC_{50} in the medium μM range (spanning from 20 to 50 μM for compounds **6a**, **6b**, **6n**, and **6m**, with PANC-1 being the most sensitive cell line to the tested compounds). An IC_{50} value was achieved for **6a**, **6b**, **6n**, **6m** compounds (Figure 11).

Additionally, tanshinone mimic **6a** could block the migration of PANC-1 and MDA-MB-231 cells (Figure 12 and Supporting Figure 8). Previously identified HuR disruptors show cytotoxic activity in cancer cell lines and in xenograft models. MS-444 induced cell death in colon cancer cells xenografted in nude mice,⁵¹ as did coumarin analogues in colon cancer cells *in vitro*.²³ Additionally, MS-444 chemo-prevented the development of intestinal tumors in APCmin mice, a model of familial adenomatous polyposis, but it was detrimental in the context of chemically induced inflammatory bowel disease (IBD). In this case, MS-444 favored azoxymethane/dextran sodium sulfate (AOM/DSS) tumorigenesis, size and invasiveness, therefore suggesting a careful evaluation of the utilization of HuR disruptors in the IBD settings.⁵² Tanshinone mimics **6a**, **6b**, **6m**, **6n**, **6k**, **6l**, and **6t** showed moderate IC_{50} in cancer cell lines, that was comparable to MS-444 (5 to 15 μM in colon cancer cell lines)⁵¹ and coumarin analogues (50 to 75 μM effective doses in colon cancer cell lines).²³ Therefore, tanshinone mimics do not affect HuR mobility directly and are endowed with interesting anti-tumor properties.

CONCLUSIONS

In our previous report, as a result of a high throughput screening on a set of anti-inflammatory agents, we identified **1**, a low-molecular-weight compound able to interact with HuR, thus affecting its post-transcriptional functions and contributing to its cytotoxic properties.²⁷ Very recently, we characterized its mechanism of action through a multidisciplinary strategy.²⁹ Here, inspired by **1** structure, we designed and synthesized an array of ortho-quinones (tanshinone mimics). They are the first family of HuR disruptors, through which the SARs reported here elucidate the steric/electrostatic requirements of a HuR binding site. In this regard, two complementary techniques, Alpha-Screen and REMSA, were used to quantify the inhibitory activity of tanshinone mimics **6a**–**t**. Among them, compounds **6a** and **6n** turned out to be more effective than **1** in HuR binding, showing a K_i of 12.8 and 15 nM respectively. In addition, **6a** is the only molecule, to our knowledge, for which a direct K_D against HuR can be measured through DMR ($K_D \approx 4.5 \mu\text{M}$). A combined approach of *in vitro* studies, NMR titration and MD simulations clarified the mechanism of action of compound **6a** that is to stabilize HuR in a peculiar closed conformation, which is incompatible with RNA binding.

From a biological point of view compound **1** inhibited viability and migration of breast cancer cell lines and induced cell death in colon cancer cells xenografted in nude mice in a HuR dependent manner,²⁹ although its pleiotropic effects contribute to its activity. The diminished cytotoxicity of tanshinone mimics compared to **1** could be ascribed to the reported multipharmacological effects of the latter,⁵³ or to limited bioavailability of tanshinone mimics. Nevertheless, our first generation tanshinone mimics are a valuable starting point to generate a more potent, *in vivo* active set of anticancer compounds. Our current efforts aim to further expanding our SARs, and to improve the efficacy of tanshinone mimics on HuR modulation in cells through the introduction of solubilizing moieties in position 1 and 7.

EXPERIMENTAL SECTION

Chemistry. Purity measurements were carried out by HPLC-MS, using NMR data to corroborate our findings. All our final compounds resulted to be $\geq 95\%$ pure.

General Procedures. ¹H NMR spectra were recorded on a Bruker Avance 400 MHz instrument in CDCl_3 , CD_3OD , or D_2O as solvent at 400 MHz. ¹³C NMR spectra were recorded in CDCl_3 , CD_3OD , or D_2O as solvent at 101 MHz. Coupling constants are given in Hertz and are rounded to the nearest 0.1 Hz. LC–MS data were collected with a Waters Acquity Ultra performance LC equipped with an Acquity UPLC HSS T3 column (2.1 mm \times 50 mm, 1.8 μm) and a SQD detector. Purifications were carried out either by flash chromatography on silica gel (particle size 60 μm , 230–400 mesh), on Kieselgel, or by Biotage flash chromatography [Biotage columns Si-25-M (150 \times 25 mm; silica gel (40–63 μm), flow rate 25 mL/min)], or by Biotage C_{18} reverse phase chromatography [Biotage column C_{18} HS (150 \times 25 mm; KP- C_{18} –HS (35–70 μm), flow rate 25 mL/min)]. Final compounds **6a**–**i**, **6k**–**p**, **6s** were purified by C_{18} reverse phase semipreparative HPLC using a Waters X-Bridge column (19 mm \times 15.0 cm, 5 μm). Melting points were determined with a Stuart Scientific SMP3 melting point apparatus. Solvents were distilled and dried according to standard procedures, and reactions requiring anhydrous conditions were performed under nitrogen or argon atmosphere.

1-Phenylsulfonyl-3-phenyl-4,5-dioxindole (6a). IBX⁴⁰ (548 mg, 1.96 mmol, 1.2 equiv) was added to a solution of 1-phenylsulfonyl-3-phenyl-5-hydroxy indole **12a** (570 mg, 1.63 mmol, 1 equiv) in EtOAc (8 mL, ≈ 0.17 M concentration), under vigorous stirring at room temperature. The reaction was monitored by TLC (eluants: *n*-Hexane/EtOAc 6/4). After 24 h, the reaction was filtered on Celite. After the

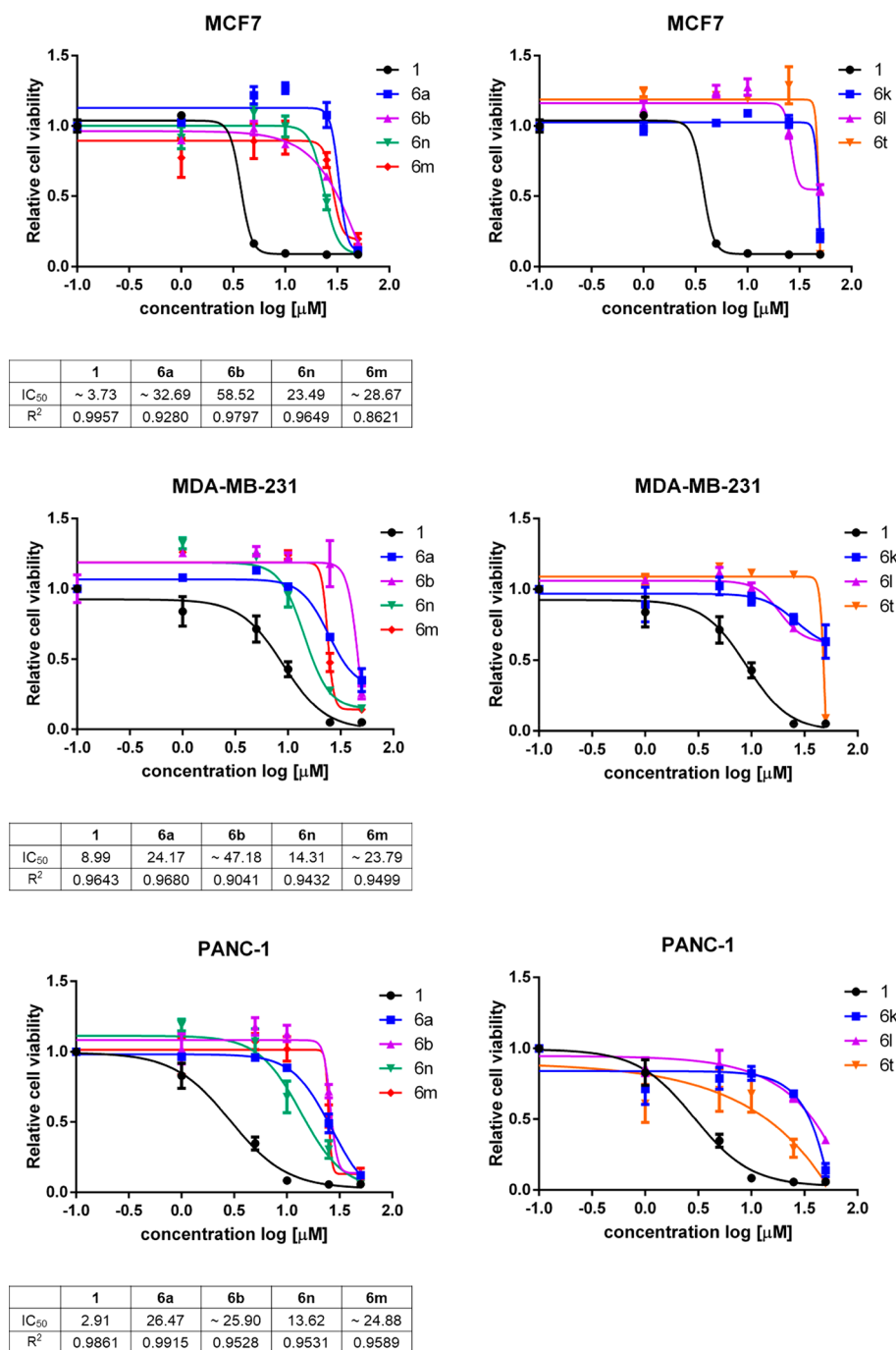


Figure 11. Cell viability of tanshinone mimics, assessed after 72 h of treatment with the indicated compounds (0–50 μM). Plotted bars are mean \pm SD of a biological duplicate, normalized to control (DMSO). Relative IC₅₀ and R² were calculated by nonlinear regression curve fitting.

solvent was concentrated, the crude (930 mg, purple solid) was purified by flash chromatography on silica gel (eluent: *n*-Hexane/EtOAc 6/4). Pure compound **6a** (515 mg, 1.42 mmol, 87% yield, \geq 95% purity) was obtained as a dark red solid, mp 140 $^{\circ}\text{C}$ (dec.). ¹H NMR (400 MHz, acetone d₆): δ (ppm) 8.25–8.23 (m, 2H, *o*-ArSO₂), 8.07 (d, 1H, *J* = 10.5 Hz, H7), 7.87 (tt, 1H, *J* = 7.5 Hz, *J* = 1.2 Hz, *p*-ArSO₂), 7.78–7.74 (m, 3H, H2, *m*-ArSO₂), 7.68–7.65 (m, 2H, *o*-Ar), 7.40–7.33 (m, 3H, *p*-Ar, *m*-Ar), 6.21 (d, 1H, *J* = 10.5 Hz, H6). ¹³C NMR (75.4 MHz, acetone d₆): δ (ppm) 182.3, 174.8, 138.5, 137.9, 136.5, 132.1, 131.5, 131.3, 130.5, 129.6, 129.1, 128.9, 128.5, 127.1. MS (ESI⁺): *m/z* 748.9 [2M+Na⁺]. Calculated MS, C₂₀H₁₃NO₄S: 363.06.

1-Alkyl/arylsulfonyl-3-phenyl-4,5-dioxoindoles, General Oxidation Procedure A (6a, 6f–h, 6l). IBX⁴⁰ (1.2 equiv) was added to a solution of 5-hydroxy indoles (1 equiv) in EtOAc (\approx 0.17 M concentration),

under vigorous stirring at room temperature. The reaction was monitored by TLC. When the reaction was completed (between 7 and 34 h), the mixture was filtered on Celite. After concentration of the solvent, the crude was purified by flash chromatography on silica gel, affording pure 1-arylsulfonyl-3-aryl-4,5-dioxo indoles as amorphous solids.

1-Arylsulfonyl-3-aryl-4,5-dioxoindoles, General Oxidation Procedure B (6b–e, 6i, 6k). IBX⁴⁰ (1.2 equiv) was added to a solution of 5-hydroxy indoles (1 equiv) in DMF (\approx 0.17 M concentration), at room temperature and under vigorous stirring. The reaction was monitored by TLC. When the reaction was completed (between 2 and 48 h), the mixture was diluted with water (20 volumes). The aqueous phase was extracted with EtOAc (10 volumes, until colorless). The collected organic layers were washed once with brine (20 volumes), dried with anhydrous Na₂SO₄, and filtered. The solvent was removed

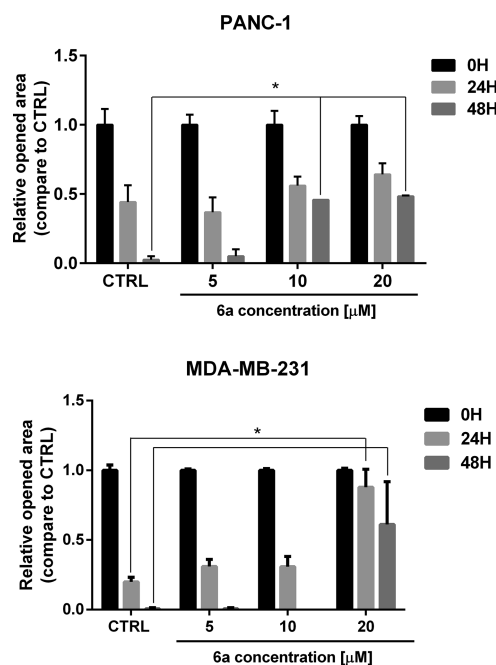


Figure 12. Scratch assay in PANC-1 and MDA-MB-231 cells. Images of invaded cells at 0, 24, and 48 h after scratching and treatment with DMSO (CTRL) or **6a** were taken from a time-lapse sequence of cell migration; wounds with consistent shape within each well were generated using a 200 μL tip. Residual open area at different time points is indicated as calculated by ImageJ software (* $p < 0.05$).

under reduced pressure, and the resulting crude was purified by flash chromatography on silica gel, affording pure 1-arylsulfonyl-3-aryl-4,5-dioxo indoles as amorphous solids.

1-Phenylsulfonyl-3-phenyl-7-thiophenyl-4,5-dioxoindole (6m). The title compound (30.2 mg, 45% yield over 2 steps, $\geq 95\%$ purity, mp 136 $^{\circ}\text{C}$ (dec.), purple solid) was prepared from 1-(phenylsulfonyl)-3-phenyl-4,5-dioxo indole **6a** (55 mg, 0.15 mmol, 1.0 equiv) and thiophenol (18.2 μL , 0.178 mmol, 1.18 equiv) in DMF (0.65 mL), following the general procedure for Michael reaction (2.5 h) and IBX oxidation. ^1H NMR (400 MHz, acetone- d_6): δ (ppm) 7.89–7.63 (m, 12H, Ar), 7.59 (s, 1H, H2), 7.42–7.31 (m, 3H, Ar), 6.91 (s, 1H, H6). ^{13}C NMR (100 MHz, acetone- d_6): δ (ppm) 177.2, 173.6, 140.3, 138.1, 137.2, 135.7, 135.6, 131.2, 130.5, 130.4, 129.1, 129.0, 128.5, 128.1, 128.0, 127.3, 122.3, 120.9, 119.5. MS (ESI $^+$): m/z 494.32 [$\text{M}+\text{Na}^+$]. Calculated MS, $\text{C}_{26}\text{H}_{17}\text{NO}_4\text{S}_2$: 471.06.

1-Phenylsulfonyl-3-phenyl-7-thioaryl-4,5-dioxoindoles, General Procedure for Michael Reaction (6m–o). A substituted thiophenol (1.18 equiv) was added to a solution of 1-(phenylsulfonyl)-3-phenyl-4,5-dioxo indole **6a** (1.0 equiv) in DMF (0.23M). The solution was stirred at room temperature for 2–3 h, then water (1 volume) was added. The mixture was extracted with EtOAc (four times, 4 volumes), and the collected organic phases were dried over sodium sulfate, filtered, and evaporated under reduced pressure. The crude was purified by reverse phase chromatography (eluent: A CH_3CN , B water, from 0% A to 100% A), affording the ortho-bisphenol (62%–88%). IBX (0.5–2 equiv) was then added to the ortho-bisphenol (1eq) in DMF (0.2 M) under stirring at rt. After reaction completion (2 h), water was added (1 volume), and the mixture was extracted with EtOAc (four times, 2 volumes). The collected organic phases were dried over sodium sulfate, filtered, and evaporated under reduced pressure. The crude residue was purified by reverse phase chromatography (eluent: A CH_3CN , B H_2O , from 0% A to 100% A) affording pure 1-(phenylsulfonyl)-3-phenyl-7-thioaryl-4,5-dioxo indoles as amorphous solids.

1-Phenylsulfonyl-3,7-diphenyl-4,5-dioxoindole (6p). The title compound (32 mg, 0.072 mmol, purple solid, 34% yield considering the recovery of 28 mg of unreacted **6a**) was obtained from 1-(phenylsulfonyl)-3-phenyl-4,5-dioxo indole **6a** (105 mg, 0.289 mmol,

1.0 equiv) and phenylboronic acid (55 mg, 0.452 mmol, 1.5 equiv) in dry DCE (3 mL, ≈ 0.09 M), following the general procedure for Mn(III)-mediated radical addition. ^1H NMR (400 MHz, DMSO d_6): δ (ppm) 8.27 (2H, d, $J = 7.7$ Hz, o-Hs of PhSO_2), 7.96 (1H, s, H2), 7.89–7.83 (2H, m, H6, p-H of PhSO_2), 7.76 (2H, t, $J = 7.7$ Hz, m-Hs of PhSO_2), 7.72–7.76 (2H, m, o-Hs of 3-Ph), 7.50–7.36 (8H, m, m- and p-Hs of 3-Ph, all Hs of 7-Ph). ^{13}C NMR (75.4 MHz, DMSO d_6): δ (ppm) 179.5, 173.4, 137.0, 136.8, 136.0, 134.9, 130.9, 130.6, 128.7, 128.3, 128.1, 127.6, 125.0, 123.8, 121.3. MS (ESI $^+$): m/z 440.21 [$\text{M}+\text{H}^+$]. Calculated MS, $\text{C}_{26}\text{H}_{17}\text{NO}_4\text{S}$: 439.09.

1-Phenylsulfonyl-3-phenyl-7-alkyl/aryl-4,5-dioxoindoles, General Procedure for Mn(III)-Mediated Radical Addition (6p–t).

1-(Phenylsulfonyl)-3-phenyl-4,5-dioxo indole **6a** (1.0 equiv) and a boronic acid (1.5 equiv) were dissolved in dry dichloroethane (DCE, ≈ 0.09 M in **6a**). The solution was stirred for 2 min and then $\text{Mn}(\text{OAc})_3 \cdot 2\text{H}_2\text{O}$ (3 equiv) was added. The mixture was kept under nitrogen atmosphere, stirred at 80 $^{\circ}\text{C}$ until reaction completion (monitoring by TLC, eluent: *n*-Hexane/EtOAc 7/3), and cooled at room temperature. Then, CH_2Cl_2 (2 volumes) and saturated aqueous NaHCO_3 (2 volumes) were added. The aqueous layer was extracted with CH_2Cl_2 (2 volumes, two times). The collected organic phases were washed with brine (8 volumes, two times), dried over sodium sulfate, filtered and evaporated under reduced pressure to give a crude solid. The crude was purified by flash chromatography (eluent: *n*-Hexane/EtOAc 7/3). Pure 1-(phenylsulfonyl)-3-phenyl-7-substituted-4,5-dioxo indoles were obtained as amorphous solids.

3-Bromo-5-methoxyindole (8). The synthesis of compound **8** was carried out as previously described,⁵⁴ and its analytical characterization confirmed its structure.

1-Phenylsulfonyl-3-phenyl-5-methoxyindole (9a). The synthesis of compound **9a** was carried out as previously described,⁵⁵ and its analytical characterization confirmed its structure.

1-Phenylsulfonyl-3-aryl-5-Substituted Indoles, General Suzuki Procedure (9b,c, 12d,e). 1-Phenylsulfonyl-3-bromo-5-methoxy- (**11**) or 5-hydroxy indole (**13**) (1 equiv) and an arylboronic acid (1.17 equiv) were placed in a two-necked round-bottom flask, equipped with a CaCl_2 valve. The flask was flushed with nitrogen to remove any trace of oxygen. The middle neck was closed by a rubber septum, then dry dimethoxyethane (DME, ≈ 0.07 M concentration in **11**) and previously deaerated aqueous 2 M K_2CO_3 (1.29 equiv) were added and the resulting mixture was stirred at room temperature under nitrogen atmosphere. Finally, PdTetrakis (0.05 equiv) and previously deaerated EtOH (final 4/1 DME/EtOH ratio) were added under nitrogen flushing. A pale yellow solution was formed. The rubber septum was removed, and then the main-middle neck was equipped with a condenser surmounted by a CaCl_2 valve. The pale yellow solution was stirred under nitrogen atmosphere, refluxed for 8 h, and left to stir at room temperature overnight. Then, the reaction mixture was diluted with a saturated solution of NH_4Cl (1 volume) and extracted with EtOAc (1.5 volumes, three times). The organic phase was washed with saturated aqueous NH_4Cl (3 volumes) and with brine (3 volumes), then dried over Na_2SO_4 and filtered. The crude was purified by flash chromatography on silica gel, affording pure 1-phenylsulfonyl-3-aryl-5-substituted indoles as amorphous solids.

1-Arylsulfonyl-3-phenyl-5-methoxyindoles, General N-Arylsulfonylation Procedure (9f–i). Aqueous 50% KOH (8 equiv) was added to a stirred mixture of 3-phenyl-5-methoxy indole **14** (1 equiv) and $n\text{-Bu}_4\text{N}^+\text{HSO}_4^-$ (0.1 equiv) in CH_2Cl_2 (≈ 0.2 M concentration in **14**). The reaction was stirred vigorously at room temperature for 10 min. An arylsulfonyl chloride (1.7 equiv) in CH_2Cl_2 (total ≈ 0.1 M concentration in **14**) was then added, and the mixture turned to orange-brown. The reaction was monitored by TLC (eluent: *n*-Hex/EtOAc 9/1). After 3 h, the reaction was stopped by diluting with water (1 volume) and extracting with CH_2Cl_2 (2 volumes, two times). The collected organic layers were washed with water (2 volumes) and brine (2 volumes), and dried over sodium sulfate. The solvent was evaporated under reduced pressure affording a crude. The crude was purified through flash chromatography on silica gel, affording pure 1-arylsulfonyl-3-phenyl-5-methoxy indoles as amorphous solids.

1-Phenylsulfonyl-3-bromo-5-methoxyindole (11). The synthesis of compound **11** was carried out as previously described,⁵⁶ and its analytical characterization confirmed its structure.

1-Phenylsulfonyl-3-phenyl-5-hydroxyindole (12a). Initially, 1 M BBr_3 in CH_2Cl_2 (26.4 mL, 6 equiv) was slowly added under nitrogen atmosphere and at -78°C to a stirred solution of 1-phenylsulfonyl-3-phenyl-5-methoxy indole **9a** (1.6 g, 4.41 mmol, 1 equiv) in dry CH_2Cl_2 (22 mL, ≈ 0.2 M concentration). The temperature was slowly increased to room temperature while monitoring by TLC (eluents: *n*-Hexane/EtOAc 8/2). The resulting dark green solution was immediately diluted with water (150 mL) and neutralized with saturated aqueous NaHCO_3 . The reaction mixture was extracted with CH_2Cl_2 (3×150 mL). The collected organic phases were then washed with brine (400 mL), dried over Na_2SO_4 , and filtered. The solvent was removed under reduced pressure. The crude (1.7 g) was purified by flash chromatography on silica gel, yielding pure compound **12a** (1.34 g, 3.84 mmol, 87% yield) as a white solid. ^1H NMR (400 MHz, acetone d_6): δ (ppm) 8.29 (s, 1H, OH), 8.05–8.03 (m, 2H, o-ArSO₂), 7.93 (d, 1H, $J = 8.9$ Hz, H7), 7.84 (s, 1H, H2), 7.69–7.65 (m, 3H, p-ArSO₂, o-Ar), 7.60–7.56 (m, 2H, m-ArSO₂), 7.50–7.46 (m, 2H, m-Ar), 7.38 (tt, 1H, $J = 7.4$ Hz, $J = 1.2$ Hz, p-Ar), 7.21 (d, 1H, $J = 2.4$ Hz, H4), 6.96 (dd, 1H, $J = 8.9$ Hz, $J = 2.4$ Hz, H6). ^{13}C NMR (75.4 MHz, acetone d_6): δ (ppm) 155.5, 138.9, 135.1, 134.0, 131.4, 130.4, 129.8, 128.6, 128.4, 127.8, 124.9, 115.6, 115.0, 106.0. MS (ESI⁺): m/z 721.0 [2M+Na⁺]. Calculated MS, $\text{C}_{20}\text{H}_{15}\text{NO}_3\text{S}$: 349.08.

1-Aryl/Alkylsulfonyl-3-Substituted-5-Hydroxyindoles, General Demethylation Procedure (12a–c, 12f–i, 12k, 12l, 13). First, 1 M BBr_3 in CH_2Cl_2 (6 equiv) was slowly added under nitrogen atmosphere and at -78°C to a stirred solution of 1-aryl/alkylsulfonyl-3-substituted-5-methoxy indoles (1 equiv) in dry CH_2Cl_2 (≈ 0.2 M concentration). The temperature was slowly increased to room temperature while monitoring by TLC, then it was immediately diluted with water (5 volumes) and neutralized with saturated aqueous NaHCO_3 . The reaction mixture was extracted with CH_2Cl_2 (5 volumes, three times). The collected organic phases were then washed with brine (15 volumes), dried over Na_2SO_4 , and filtered. The solvent was removed under reduced pressure. The crude hydroxyl indoles were purified by flash chromatography on silica gel, affording pure 1-aryl/alkylsulfonyl-3-substituted-5-hydroxy indoles as amorphous solids.

3-Phenyl-5-methoxyindole (14). Aqueous 3 M NaOH (21 mL, 63 mmol, 46 equiv) was added dropwise in 30 min to a solution of 1-phenylsulfonyl-3-phenyl-5-methoxy indole **9a** (500 mg, 1.38 mmol, 1 equiv) in 2/1 MeOH/THF (207 mL). The pale pink mixture was warmed up to 80°C . The reaction was monitored by TLC (eluant: *n*-Hex/EtOAc 8/2). After 2 h the reaction was stopped by acidifying with 3 N HCl (21 mL), and the organic solvents were evaporated under reduced pressure. The aqueous residue was extracted with EtOAc (3×100 mL). The collected organic layers were washed with brine (450 mL), and dried over sodium sulfate. The solvent was evaporated under reduced pressure affording a crude brown oil (365 mg), that was purified by flash chromatography on silica gel (eluant: *n*-Hex/EtOAc 85/15). Pure compound **14** (300 mg, 1.34 mmol, 97% yield) was obtained as a pale yellow solid. ^1H NMR (400 MHz, acetone d_6): δ (ppm) 10.33 (1H, bs, NH), 7.72–7.69 (2H, m, o-Ar), 7.58 (1H, d, $J = 2.6$ Hz, H2), 7.47–7.36 (4H, m, H4, H7, m-Ar), 7.26–7.21 (1H, m, p-Ar), 6.85 (1H, dd, $J = 2.50$ Hz, $J = 8.80$ Hz, H6), 3.84 (3H, s, OMe). MS (ESI⁺): m/z 748.9 [2M+Na⁺]. Calculated MS, $\text{C}_{15}\text{H}_{13}\text{NO}$: 223.27.

Biology. Amplified Luminescent Proximity Homogeneous Assay (ALPHA Screen). AlphaScreen assays have been performed using histidine (nickel) chelate detection kit (PerkinElmer, 6760619), based on the reaction of an His-tagged HuR protein and a biotinylated single strand RNA (BITEG-RNA), as previously described.²⁸ The full-length HuR recombinant protein has been expressed in *E. coli* Rosetta DH5a according to an already published protocol.²⁷ Hooking point curves, with 50 nM of BITEG-RNA probe, have been performed to test its activity after purification and dialysis. Dissociation equilibrium constants (K_d) were calculated with respect to a K_D of 2.5 nM for the Bi–AU ligand interaction, in the presence of as low as 0.5% DMSO (relative control) and of tanshinone mimics. Non specific interference with the assay has been evaluated by reacting the same amount of acceptor and donor

beads (20 $\mu\text{g}/\text{mL}/\text{well}$) with biotinylated-His₆ molecule in the same experimental conditions. GraphPad Prism software v5.1 has been used for fitting calculation and statistical significance. rHuR expressed in HEK293T has been purified according to a previously published protocol.²⁷

RNA-Electrophoretic Mobility Shift Assays (REMSAs). REMSAs were performed as previously indicated,²⁷ with minor modifications. Besides recombinant full-length HuR, HuR RRM1–2 and RRM3 constructs were used to express and purify proteins as previously described.^{27,29}

At least 10-fold excess of recombinant HuR and its RRMs were incubated for 30 min with either 75 fmol of 5'-DY681-labeled AU-rich RNA probe or with 25 nM of 5'-FAM-labeled RNA probe or with 500 nM of Cy-3-RNA probe and DMSO as control or tanshinone mimics at their reference doses. Then samples were loaded on 4% native polyacrylamide gel, image was developed with Odyssey infrared Imaging System (LI-COR Biosciences) for DY681-labeled RNA or in Typhoon Trio scanner (GE Healthcare) at high resolution for FAM and Cy-3 probe.

Dynamic Mass Redistribution (DMR). The EnSight Multimode Plate Reader (PerkinElmer) was used to perform DMR analyses. Full-length HuR protein (15 $\mu\text{L}/\text{well}$ of a 50 $\mu\text{g}/\text{mL}$ HuR solution in 20 mM sodium acetate buffer, pH 5.5) was immobilized on label-free microplate (EnSpire-LFB high sensitivity microplates) by amine-coupling chemistry, incubating the microplate o/n at 4°C . Importantly, each well contains a reactive area, containing chemical groups to allow amine coupling reaction, and empty area. After the initial step of immobilization, the unbound protein was washed away and the plate equilibrated using the assay buffer (HEPES 25 mM pH 8, 3 mM MgCl_2 , 100 mM NaCl, 8% Glycerol, 0.05% BSA, 0.005% Tween20). Next, the interaction between tanshinone mimics, diluted to different concentrations in the same buffer, and HuR protein was monitored during 30 min at room temperature. The EnSight software (Kaleido) acquires data by automatically subtracting the signal in the empty area from the one of the reactive area. Binding response is then calculated by subtracting the baseline read from the final read. This dual-control strategy guarantees that nonspecific signals arising from the potential interaction of the HuR protein with the surface of the plate are already subtracted in each well. All the steps were executed by employing a Zephyr Compact Liquid Handling Workstation. The Kaleido software was used to acquire and process the data.

Circular Dichroism Experiments. All experiments has been done by using a final 10 μM concentration of TNF-ARE and 10 μM **6a**, 10 mM in sodium phosphate buffer pH 7.3. CD spectra were measured in a JASCO-700 Spectrophotometer at 240–350 nm range (DMSO interfered below 240 nm), at 100 nm/min speed. Next 10 μM **6a** dissolved in sodium phosphate buffer pH 7.3 was also measured separately to exclude background from the **6a** (10 μM) + TNF ARE (10 μM) spectra. The analyzed spectra $\Delta\epsilon$ was then plotted using the Graphpad Prism 6 plotting tool.

Cell Culture. Human breast adenocarcinoma MCF7 (ICLC; HTL95021) and MDA-MB-231 (ICLC; HTL99004) and pancreatic carcinoma PANC-1 (kindly provided by G. Feldmann)⁵⁷ cell lines were cultured in high glucose Dulbecco's modified Eagle's medium (DMEM) supplemented with 10% fetal bovine serum (FBS, Lonza), 2 mM L-glutamine, 100 U/ml penicillin-streptomycin (Lonza) in standard growth conditions.

RIP and qRT-PCR. Five million MCF7 cells/sample were used for each RIP experiment, performed as previously described,⁵⁸ without cross-linking steps and using 1 $\mu\text{g}/\text{mL}$ of anti-HuR antibody (Santa Cruz, 71290) or of mouse IgG isotype (negative control, Santa Cruz 2025). TRIzol reagent was added directly to the beads for HuR-bound RNA isolation and processed for qRT-PCR analysis. Quantitative PCRs, after cDNA Synthesis (Thermo Scientific, K1612) were performed using Universal SYBR Master Mix (KAPA Biosystems, KR0389) on CFX-96/384 thermal cyclers (BIO-RAD), as previously described.²⁷ Fold enrichment was determined using the eq 2- $\Delta\Delta\text{Ct}$, where the Ct value for HuR and IgG IP was subtracted from the Ct value of the housekeeping gene RPLP0 to yield the ΔCt value. For each condition, ΔCt value for the HuR and IgG IP sample were calculated in triplicate. The delta Ct value for HuR in the IgG IP samples were calculated in the same way. Then delta–delta Ct values

were calculated from the difference between HuR IP samples and IgG IP samples. Total expression level of the different mRNAs was assessed by extracting total RNA from the control and treated samples and then qRT-PCRs have been performed as described previously. The sequence of the primer used for each PCR are the following:

gene	primer sequence FW 5'-3'	primer sequence RV 5'-3'
RPLP0	CATTCTCGCTT- CCTGGAG	CTTGACCTTTTCAGC- AAGTGG
ERBB2	GGTACTGAAAG- CCTTAGGGAAGC	ACACCATTGCTGTTC- CTTCCTC
VEGFA	CCGCAGACGTG- TAAATGTTCTC	CGGCTTGTCACATCT- GCAAGTA
CTNNB1	GACCTCATGGA- TGGGCTGCCT	GATTTACAAATAGCC- TAAACCAC
RNA18s	GCAGCTAGGAA- TAATGGAATAG	TGGCAAATGCTTTTCG- CTCTG
HPRT1	TGACACTGGCA- AAACAATGCA	GGTCCTTTTCACCAG- CAAGCT

Immunofluorescence Experiments. 8.000 MCF7 cells/well were seeded in a 96-well plate and treated with 1 μ M of **1**, or 10 μ M of tanshinone mimics, or 2.5 μ M of ActD (Sigma A1410) for 3 h and were fixed with 3.7% paraformaldehyde (PFA) for 15 min at RT. Cells were treated for 10 min with permeabilization buffer (200 mM sucrose, 0.2% Triton X-100) followed by blocking for 15 min with blocking buffer (2% Bovine Serum Albumin in PBS). Primary antibody anti-HuR 1:250 in 3% BSA and secondary fluorophore conjugated (Alexa 594 Red) antibody (1:500) were diluted in PBS + BSA 0.6%. DAPI Blue (1.5 μ g/mL) in PBS + BSA 0.6% was used to detect nuclei. PerkinElmer image plate reader Operetta was used for image acquisition and evaluation by selecting 13 fields/well. The ratio between nuclear and cytoplasmic signal represents the mean of single cells for every well.

Cell Viability Assay. To test cell viability, cells were grown and treated in 96 well-plate for 48 h. Cells were then assayed using OZBlue Cell Viability kit (Oz Biosciences, BL000). In brief, OZBlue was added at 10% volume of culture media to each well and cells were further incubated for 3 h at 37 °C. Fluorescence was then determined (excitation 560 and emission 590 nm) by a Tecan microplate reader. Cell survival was calculated with respect to control (DMSO), and IC₅₀ values were determined by fitting with GraphPad Prism software v5.1.

Cell Migration Assay. Cells were seeded for migration assay and treated with tanshinone mimics as previously described.⁵⁹ Images of the same field were acquired immediately ($t = 0$), after 24 and 48 h using a Leica DM IL Led microscope (5 \times magnification) and wounded-open areas were measured using ImageJ software.

Statistical Analysis. All data are expressed as means \pm SD from at least two independent experiments. Magnitude of significance was evaluated by student *t* test and probability (*P*) values <0.05, < 0.01, and <0.001 were indicated with *, **, *** symbols, respectively.

In Silico Pan Assay Interference, NMR, and Molecular Modeling studies. *In Silico Pan Assay Interference.* All compounds as reported in Table 1 were screened for Pan Assay Interference using the PAINS-Remover Web server (<http://www.cbligand.org>). All compounds passed this filtering.

NMR Measurements on Protein/Compound 6a Interaction. The assignment of RRM1-RRM2 tandem domains of HuR was previously reported (BMRB code: 27002).⁵⁰ The effect of the tanshinone mimic **6a** on the RRM1-RRM2 tandem domains of HuR (100 μ M) has been evaluated in the following experimental conditions: 20 mM Tris-Cl, pH 8, 10 mM Gly, 50 mM NaCl. 2D ¹H ¹⁵N HSQC spectra were acquired at 298 K on Bruker Avance 900 MHz NMR spectrometer to monitor the effect of increasing amounts of the ligand (HuR/compound **6a** molar ratio of 1:0.2, 1:0.4, 1:0.6, 1:0.8, 1:1, 1:2) added to the protein solution.

Docking Calculations. Molecular docking was carried out using the Glide 6.5⁶⁰ and the AutoDock 4.2⁶¹ software. **6a** three-dimensional structure was first generated and subsequently prepared through the LigPrep module, as implemented in the Maestro 10.0.013 graphical user interface.⁶² As experimental results suggest that (I) HuR cannot bind both

6a and RNA at the same time and that (II) **6a** stabilizes HuR in a "closed" conformation, we selected as receptor structure for docking calculations the structure of the HuR–mRNA complex (PDB ID: 4EDS),⁴⁹ and removed the RNA strand. Indeed this structure was not only the HuR highest resolution structure available but also the best representative structure of a HuR "closed" form available. Receptor structure was then prepared through the Protein Preparation Wizard, also implemented in Maestro, and the OPLS-2005 force field. Water molecules and residual crystallographic buffer components were removed, missing side chains were built using the Prime module, hydrogen atoms were added, side chains protonation states at pH 7.0 were assigned and, finally, minimization was performed until the RMSD of all the heavy atoms was within 0.3 Å of the crystallographically determined positions. In both cases, the binding pocket was identified by placing a cube centered in proximity of the "hinge" loop between the RRM1 and RRM2 domains. Docking calculations were performed as following. Docking with Glide was carried out in extra-precision (XP) mode, using GlideScore for ligand ranking. The inner box size was chosen to be 40 Å in all directions and the size of the outer box was set by choosing a threshold length for the ligand size to be docked of 30 Å. A maximum of 100 000 poses per ligand was set to pass to the grid refinement calculation, and the best 10 000 poses were kept for the energy minimization step. The maximum number of poses per ligand to be outputted was set to 10. In the case of docking with Autodock, the ligand and receptor structures were first converted to AD4 format files, adopting the Gasteiger-Marsili partial charges, via AutoDockTools.⁶¹ The box size was set to have 117 \times 125 \times 127 points in the three-dimensional space with a Grid spacing of 0.481 Å per point using AutoGrid 4.2. A hundred independent runs of the Lamarckian genetic algorithm local search (GALS) method per docking calculation were performed, by applying a threshold of maximum 10 million energy evaluations per run. The rest of the docking parameters was set as default. Docking conformations were clustered on the basis of their RMSD (tolerance = 2.0 Å) and were ranked according to the AutoDock scoring function. In both cases, the box size was chosen so as to encompass the whole RNA binding surface of HuR.

Molecular Dynamics Simulations and Analyses. The best ranked HuR–**6a** complexes, as issuing from the docking calculations, were submitted to MD simulations with NAMD,⁶³ using the ff99SBildn Amber force field parameters,^{64,65} for protein and the parameters recently developed by Allnér and co-workers for ions.⁶⁶ Parameters for **6a** were generated in two steps. Initially, charges were computed using the restrained electrostatic potential (RESP) fitting procedure.⁶⁷ The ESP was first calculated by means of the Gaussian09 package⁶⁸ using a 6-31G* basis set at Hartree–Fock level of theory, and then the RESP charges were obtained by a two-stages fitting procedure using the program RED.^{69,70} Missing bond, angle, torsion, and improper torsion angle parameters were then generated using Antechamber.⁷¹ The complex was then solvated in a 15 Å layer cubic water box using the TIP3P water model parameters. Neutrality was reached by adding five further Cl⁻ ions. The final system size was \sim 75 Å \times 74 Å \times 93 Å for a total number of atoms of \sim 48 000. A 10 Å cutoff (switched at 8.0 Å) was used for atom pair interactions. The long-range electrostatic interactions were computed by means of the particle mesh Ewald (PME) method using a 1.0 Å grid spacing in periodic boundary conditions. The RATTLE algorithm was applied to constrain bonds involving hydrogen atoms, and thus a 2 fs integration time step could be used. The system was minimized in two stages: first, a 20 000-step run was carried out with restraints on all the protein and ligand atoms (5 kcal/mol/Å²); then, a further 10 000-step minimization was carried out by applying restraints on the ligand and C α protein atoms only. A 2 ns NPT simulation at 200 K and 1 atm was performed with restraints on all the protein atoms (5 kcal/mol/Å²), to adjust the volume of the simulation box, while preserving the minimized protein structure obtained in the previous steps. Afterward, the system was slowly heated up to 300 K over a 3 ns period, gradually releasing the restraints (on the ligand and protein C α atoms only) to 1 kcal/mol/Å² along the thermalization process. Subsequently, the system was equilibrated for 2 ns, gradually reducing the restraints to zero. Production runs were then performed under NPT conditions at 1 atm and 300 K. Each

of the four simulations was extended up to 1.5 μ s. MD trajectory visualization and RMSD analysis were performed by means of the VMD software.⁷² All other analyses were performed using CPPTRAJ⁷³ or in-house scripts exploiting the MDAnalysis library.⁷⁴ For analysis purposes, trajectories were fitted onto the β -sheet backbone atoms, owing to the HuR high overall flexibility, using the first frame as reference and then one frame each 100 ps. In the specific case of contact analysis only, we employed a different reference structure. Indeed, as the aim of the analysis was also to discriminate between contacts established in the HuR mRNA-bound conformation and possible contacts characteristic of new **6a**-induced conformations, we made a distinction between native and non-native contacts. A non-native contact, contrarily to a native contact, is a contact between atoms within a convenient distance (here 4 Å) that is not present in a certain reference structure (here the structure used for the docking calculations). Figures were generated using the UCSF-Chimera software package⁷⁵ or in-house scripts with Matplotlib.⁷⁶

■ ASSOCIATED CONTENT

Supporting Information

The Supporting Information is available free of charge on the ACS Publications website at DOI: 10.1021/acs.jmedchem.7b01176.

Synthetic protocols and analytical characterization (NMR and HPLC-MS) for final compounds **6b–6k**, **6n–6o**, **6q–6w** and for synthetic intermediates. Availability of molecular formula strings. Supporting Figures S1–S8 are, respectively, related to the activity of compound **1** and **6a** with the rHuR produced in HEK293T, REMSA assays for tanshinone mimics, RMSD of MD simulations, and cell migration assays. Supporting Table 1, containing primary data from cell viability assays on tanshinone mimics (PDF) Structural animation (MPG) Compound data (CSV)

■ AUTHOR INFORMATION

Corresponding Authors

*E-mail for P.S.: pierfausto.seneci@unimi.it. Tel: +39 02-50314060. Fax: +39 02-50314074.

*E-mail for L.M.: lmarinel@unina.it. Tel: +39 081-679899. Fax: +39 081 676569.

*E-mail for A.P.: alessandro.provenzani@unitn.it. Tel: +390461283176. Fax: +390461283239.

ORCID

Leonardo Manzoni: 0000-0002-2056-8459

Ettore Novellino: 0000-0002-2181-2142

Luciana Marinelli: 0000-0002-4084-8044

Author Contributions

[○]L.M., C.Z., and D.D.M. contributed equally.

Notes

The authors declare the following competing financial interest(s): The molecules herein reported are present in patents: Italian Patent 151367 and PCT/IB2017/053519.

■ ACKNOWLEDGMENTS

Associazione Italiana per la Ricerca sul Cancro (AIRC) [17153 to A.P.]

■ ABBREVIATIONS USED

CAN, cerium ammonium nitrate; DDQ, 2,3-dichloro-5,6-dicyano-1,4-benzoquinone; DHTS, Dihydratanshinone I; DME, dimethoxyetane; DMF, dimethylformamide; EtOAc, ethyl acetate; FOS, function-oriented synthesis; HuR, human

antigene R; IBX, 2-iodoxybenzoic acid; MeCN, acetonitrile; NMR, nuclear magnetic resonance; THF, tetrahydrofuran

■ REFERENCES

- (1) Keene, J. D. RNA Regulons: Coordination of Post-Transcriptional Events. *Nat. Rev. Genet.* **2007**, *8* (7), 533–543.
- (2) Brennan, C. M.; Steitz, J. a. HuR and mRNA Stability. *Cell. Mol. Life Sci.* **2001**, *58* (2), 266–277.
- (3) Latorre, E.; Carelli, S.; Raimondi, I.; D'Agostino, V.; Castiglioni, I.; Zucal, C.; Moro, G.; Luciani, A.; Ghilardi, G.; Monti, E.; Inga, A.; Di Giulio, A. M.; Gorio, A.; Provenzani, A. The Ribonucleic Complex HuR-MALAT1 Represses CD133 Expression and Suppresses Epithelial-Mesenchymal Transition in Breast Cancer. *Cancer Res.* **2016**, *76* (9), 2626–2636.
- (4) Izquierdo, J. M. Hu Antigen R (HuR) Functions as an Alternative Pre-mRNA Splicing Regulator of Fas Apoptosis-Promoting Receptor on Exon Definition. *J. Biol. Chem.* **2008**, *283* (27), 19077–19084.
- (5) Mukherjee, N.; Corcoran, D. L.; Nusbaum, J. D.; Reid, D. W.; Georgiev, S.; Hafner, M.; Ascano, M.; Tuschl, T.; Ohler, U.; Keene, J. D. Integrative Regulatory Mapping Indicates That the RNA-Binding Protein HuR Couples Pre-mRNA Processing and mRNA Stability. *Mol. Cell* **2011**, *43* (3), 327–339.
- (6) Al-Ahmadi, W.; Al-Ghamdi, M.; Al-Haj, L.; Al-Saif, M.; Khabar, K. S. A. Alternative Polyadenylation Variants of the RNA Binding Protein, HuR: Abundance, Role of AU-Rich Elements and Auto-Regulation. *Nucleic Acids Res.* **2009**, *37* (11), 3612–3624.
- (7) Lebedeva, S.; Jens, M.; Theil, K.; Schwanhäusser, B.; Selbach, M.; Landthaler, M.; Rajewsky, N. Transcriptome-Wide Analysis of Regulatory Interactions of the RNA-Binding Protein HuR. *Mol. Cell* **2011**, *43* (3), 340–352.
- (8) Katsanou, V.; Papadaki, O.; Milatos, S.; Blackshear, P. J.; Anderson, P.; Kollias, G.; Kontoyiannis, D. L. HuR as a Negative Posttranscriptional Modulator in Inflammation. *Mol. Cell* **2005**, *19* (6), 777–789.
- (9) Wang, W.; Caldwell, M. C.; Lin, S.; Furneaux, H.; Gorospe, M. HuR Regulates Cyclin A and Cyclin B1 mRNA Stability during Cell Proliferation. *EMBO J.* **2000**, *19*, 2340–2350.
- (10) Abdelmohsen, K.; Pullmann, R.; Lal, A.; Kim, H. H.; Galban, S.; Yang, X.; Blethrow, J. D.; Walker, M.; Shubert, J.; Gillespie, D. a.; Furneaux, H.; Gorospe, M. Phosphorylation of HuR by Chk2 Regulates SIRT1 Expression. *Mol. Cell* **2007**, *25* (4), 543–557.
- (11) Abdelmohsen, K.; Gorospe, M. Posttranscriptional Regulation of Cancer Traits by HuR. *Wiley Interdiscip. Rev. RNA* **2010**, *1* (2), 214–229.
- (12) Levy, N. S.; Chung, S.; Furneaux, H.; Levy, A. P. Hypoxic Stabilization of Vascular Endothelial Growth Factor mRNA by the RNA-Binding Protein HuR. *J. Biol. Chem.* **1998**, *273* (11), 6417–6423.
- (13) Tang, K.; Breen, E. C.; Wagner, P. D. Hu Protein R-Mediated Posttranscriptional Regulation of VEGF Expression in Rat Gastrocnemius Muscle. *Am. J. Physiol. Heart Circ. Physiol.* **2002**, *283* (4), H1497–H1504.
- (14) Akool, E.-S.; Kleinert, H.; Hamada, F. M. A.; Abdelwahab, M. H.; Förstermann, U.; Pfeilschifter, J.; Eberhardt, W. Nitric Oxide Increases the Decay of Matrix Metalloproteinase 9 mRNA by Inhibiting the Expression of mRNA-Stabilizing Factor HuR. *Mol. Cell. Biol.* **2003**, *23* (14), 4901–4916.
- (15) Wang, W.; Yang, X.; Cristofalo, V. J.; Holbrook, N. J.; Gorospe, M. Loss of HuR Is Linked to Reduced Expression of Proliferative Genes during Replicative Senescence. *Mol. Cell. Biol.* **2001**, *21* (17), 5889–5898.
- (16) Ishimaru, D.; Ramalingam, S.; Sengupta, T. K.; Bandyopadhyay, S.; Dellis, S.; Tholanikunnel, B. G.; Fernandes, D. J.; Spicer, E. K. Regulation of Bcl-2 Expression by HuR in HL60 Leukemia Cells and A431 Carcinoma Cells. *Mol. Cancer Res.* **2009**, *7* (8), 1354–1366.
- (17) Abdelmohsen, K.; Lal, A.; Kim, H. H.; Gorospe, M. Posttranscriptional Orchestration of an Anti-Apoptotic Program by HuR. *Cell Cycle* **2007**, *6* (11), 1288–1292.

- (18) Kafasla, P.; Skliris, A.; Kontoyiannis, D. L. Post-Transcriptional Coordination of Immunological Responses by RNA-Binding Proteins. *Nat. Immunol.* **2014**, *15* (6), 492–502.
- (19) Atasoy, U.; Watson, J.; Patel, D.; Keene, J. D. ELAV Protein HuA (HuR) Can Redistribute between Nucleus and Cytoplasm and Is Upregulated during Serum Stimulation and T Cell Activation. *J. Cell Sci.* **1998**, *111*, 3145–3156.
- (20) Galbán, S.; Kuwano, Y.; Pullmann, R.; Martindale, J. L.; Kim, H. H.; Lal, A.; Abdelmohsen, K.; Yang, X.; Dang, Y.; Liu, J. O.; Lewis, S. M.; Holcik, M.; Gorospe, M. RNA-Binding Proteins HuR and PTB Promote the Translation of Hypoxia-Inducible Factor 1 α . *Mol. Cell Biol.* **2008**, *28* (1), 93–107.
- (21) Zucal, C.; D'Agostino, V.; Loffredo, R.; Mantelli, B.; Thongon, N.; Lal, P.; Latorre, E.; Provenzani, A. Targeting the Multifaceted HuR Protein, Benefits and Caveats. *Curr. Drug Targets* **2015**, *16* (5), 499–515.
- (22) Meisner, N.-C.; Hintersteiner, M.; Mueller, K.; Bauer, R.; Seifert, J.-M.; Naegeli, H.-U.; Ottl, J.; Oberer, L.; Guenat, C.; Moss, S.; Harrer, N.; Woisetschlaeger, M.; Buehler, C.; Uhl, V.; Auer, M. Identification and Mechanistic Characterization of Low-Molecular-Weight Inhibitors for HuR. *Nat. Chem. Biol.* **2007**, *3* (8), 508–515.
- (23) Wu, X.; Lan, L.; Wilson, D. M.; Marquez, R. T.; Tsao, W.-C.; Gao, P.; Roy, A.; Turner, B. A.; McDonald, P.; Tunge, J. A.; Rogers, S. A.; Dixon, D. A.; Aubé, J.; Xu, L. Identification and Validation of Novel Small Molecule Disruptors of HuR-mRNA Interaction. *ACS Chem. Biol.* **2015**, *10* (6), 1476–1484.
- (24) Wang, Z.; Bhattacharya, A.; Ivanov, D. N. Identification of Small-Molecule Inhibitors of the HuR/RNA Interaction Using a Fluorescence Polarization Screening Assay Followed by NMR Validation. *PLoS One* **2015**, *10* (9), e0138780.
- (25) Chae, M.-J.; Sung, H. Y.; Kim, E.-H.; Lee, M.; Kwak, H.; Chae, C. H.; Kim, S.; Park, W.-Y. Chemical Inhibitors Destabilize HuR Binding to the AU-Rich Element of TNF- α mRNA. *Exp. Mol. Med.* **2009**, *41* (11), 824–831.
- (26) Kwak, H.; Jeong, K.-C.; Chae, M.-J.; Kim, S.-Y.; Park, W.-Y. Flavonoids Inhibit the AU-Rich Element Binding of HuC. *BMB Rep.* **2009**, *42* (1), 41–46.
- (27) D'Agostino, V. G.; Lal, P.; Mantelli, B.; Tiedje, C.; Zucal, C.; Thongon, N.; Gaestel, M.; Latorre, E.; Marinelli, L.; Seneci, P.; Amadio, M.; Provenzani, A. Dihydrotanshinone-I Interferes with the RNA-Binding Activity of HuR Affecting Its Post-Transcriptional Function. *Sci. Rep.* **2015**, *5*, 16478.
- (28) D'Agostino, V. G.; Adami, V.; Provenzani, A. A Novel High Throughput Biochemical Assay to Evaluate the HuR Protein-RNA Complex Formation. *PLoS One* **2013**, *8* (8), e72426.
- (29) Lal, P.; Cerofolini, L.; D'Agostino, V. G.; Zucal, C.; Fuccio, C.; Bonomo, I.; Dassi, E.; Giuntini, S.; Di Maio, D.; Vishwakarma, V.; Preet, R.; Williams, S. N.; Fairlamb, M. S.; Munk, R.; Lehrmann, E.; Abdelmohsen, K.; Elezgarai, S. R.; Luchinat, C.; Novellino, E.; Quattrone, A.; Biasini, E.; Manzoni, L.; Gorospe, M.; Dixon, D. A.; Seneci, P.; Marinelli, L.; Fragai, M.; Provenzani, A. Regulation of HuR Structure and Function by Dihydrotanshinone-I. *Nucleic Acids Res.* **2017**, *45* (16), 9514–9527.
- (30) Kaur, K.; Wu, X.; Fields, J. K.; Johnson, D. K.; Lan, L.; Pratt, M.; Somoza, A. D.; Wang, C. C. C.; Karanicolos, J.; Oakley, B. R.; Xu, L.; De Guzman, R. N. The Fungal Natural Product Azaphilone-9 Binds to HuR and Inhibits HuR-RNA Interaction in Vitro. *PLoS One* **2017**, *12* (4), e0175471.
- (31) Nasti, R.; Rossi, D.; Amadio, M.; Pascale, A.; Unver, M. Y.; Hirsch, A. K. H.; Collina, S. Compounds Interfering with Embryonic Lethal Abnormal Vision (ELAV) Protein:RNA Complexes: An Avenue for Discovering New Drugs. *J. Med. Chem.* **2017**, *60* (20), 8257–8267.
- (32) Wang, H.; Zeng, F.; Liu, Q.; Liu, H.; Liu, Z.; Niu, L.; Teng, M.; Li, X. The Structure of the ARE-Binding Domains of Hu Antigen R (HuR) Undergoes Conformational Changes during RNA Binding. *Acta Crystallogr., Sect. D: Biol. Crystallogr.* **2013**, *69*, 373–380.
- (33) Scheiba, R. M.; de Opakua, A. I.; Díaz-Quintana, A.; Cruz-Gallardo, I.; Martínez-Cruz, L. A.; Martínez-Chantar, M. L.; Blanco, F. J.; Díaz-Moreno, I. The C-Terminal RNA Binding Motif of HuR Is a Multi-Functional Domain Leading to HuR Oligomerization and Binding to U-Rich RNA Targets. *RNA Biol.* **2014**, *11* (10), 1250–1261.
- (34) Díaz-Quintana, A.; García-Mauriño, S. M.; Díaz-Moreno, I. Dimerization Model of the C-Terminal RNA Recognition Motif of HuR. *FEBS Lett.* **2015**, *589* (10), 1059–1066.
- (35) Zhou, L.; Zuo, Z.; Chow, M. S. S. Danshen: An Overview of Its Chemistry, Pharmacology, Pharmacokinetics, and Clinical Use. *J. Clin. Pharmacol.* **2005**, *45* (12), 1345–1359.
- (36) Wilson, R. M.; Danishefsky, S. J. Small Molecule Natural Products in the Discovery of Therapeutic Agents: The Synthesis Connection. *J. Org. Chem.* **2006**, *71* (22), 8329–8351.
- (37) Wender, P. A.; Quiroz, R. V.; Stevens, M. C. Function through Synthesis-Informed Design. *Acc. Chem. Res.* **2015**, *48* (3), 752–760.
- (38) Crane, E. A.; Gademann, K. Capturing Biological Activity in Natural Product Fragments by Chemical Synthesis. *Angew. Chem., Int. Ed.* **2016**, *55* (12), 3882–3902.
- (39) Cheng, Y.-C.; Liou, J.-P.; Kuo, C.-C.; Lai, W.-Y.; Shih, K.-H.; Chang, C.-Y.; Pan, W.-Y.; Tseng, J. T.; Chang, J.-Y. MPT0B098, a Novel Microtubule Inhibitor That Destabilizes the Hypoxia-Inducible Factor-1 α mRNA through Decreasing Nuclear-Cytoplasmic Translocation of RNA-Binding Protein HuR. *Mol. Cancer Ther.* **2013**, *12* (7), 1202–1212.
- (40) Fujiwara, Y.; Domingo, V.; Seiple, I. B.; Gianatassio, R.; Del Bel, M.; Baran, P. S. Practical C-H Functionalization of Quinones with Boronic Acids. *J. Am. Chem. Soc.* **2011**, *133* (10), 3292–3295.
- (41) Frigerio, M.; Santagostino, M.; Sputore, S. A User-Friendly Entry to 2-Iodoxybenzoic Acid (IBX). *J. Org. Chem.* **1999**, *64* (12), 4537–4538.
- (42) Dickschat, A.; Studer, A. Radical Addition of Arylboronic Acids to Various Olefins under Oxidative Conditions. *Org. Lett.* **2010**, *12* (18), 3972–3974.
- (43) Lee, J.; Snyder, J. K. Ultrasound-Promoted Cycloadditions in the Synthesis of Salvia Miltiorrhiza Abietanoid O-Quinones. *J. Org. Chem.* **1990**, *55* (17), 4995–5008.
- (44) Eglén, R. M.; Reisine, T.; Roby, P.; Rouleau, N.; Illy, C.; Bossé, R.; Bielefeld, M. The Use of AlphaScreen Technology in HTS: Current Status. *Curr. Chem. Genomics* **2008**, *1*, 2–10.
- (45) Schorpp, K.; Rothenaigner, I.; Salmina, E.; Reinshagen, J.; Low, T.; Brenke, J. K.; Gopalakrishnan, J.; Tetko, I. V.; Gul, S.; Hadian, K. Identification of Small-Molecule Frequent Hitters from AlphaScreen High-Throughput Screens. *J. Biomol. Screening* **2014**, *19* (5), 715–726.
- (46) Massignan, T.; Cimini, S.; Stincardini, C.; Cerovic, M.; Vanni, I.; Elezgarai, S. R.; Moreno, J.; Stravalaci, M.; Negro, A.; Sangiovanni, V.; Restelli, E.; Riccardi, G.; Gobbi, M.; Castilla, J.; Borsello, T.; Nonno, R.; Biasini, E. A Cationic Tetrapyrrole Inhibits Toxic Activities of the Cellular Prion Protein. *Sci. Rep.* **2016**, *6* (1), 23180.
- (47) Latorre, E.; Castiglioni, I.; Gatto, P.; Carelli, S.; Quattrone, A.; Provenzani, A. Loss of Protein Kinase C δ /HuR Interaction Is Necessary to Doxorubicin Resistance in Breast Cancer Cell Lines. *J. Pharmacol. Exp. Ther.* **2014**, *349* (1), 99–106.
- (48) Mujo, A.; Lixa, C.; Carneiro, L. A. M.; Anobom, C. D.; Almeida, F. C.; Pinheiro, A. S. ¹H, ¹⁵N and ¹³C Resonance Assignments of the RRM1 Domain of the Key Post-Transcriptional Regulator HuR. *Biomol. NMR Assignments* **2015**, *9* (2), 281–284.
- (49) Benoit, R. M.; Meisner, N.-C.; Kallen, J.; Graff, P.; Hemmig, R.; Cèbe, R.; Ostermeier, C.; Widmer, H.; Auer, M. The X-Ray Crystal Structure of the First RNA Recognition Motif and Site-Directed Mutagenesis Suggest a Possible HuR Redox Sensing Mechanism. *J. Mol. Biol.* **2010**, *397* (5), 1231–1244.
- (50) Sigurdardóttir, A. G.; Winter, A.; Sobkowitz, A.; Fragai, M.; Chirgadze, D.; Ascher, D. B.; Blundell, T. L.; Gherardi, E. Exploring the Chemical Space of the Lysine-Binding Pocket of the First Kringle Domain of Hepatocyte Growth Factor/scatter Factor (HGF/SF) Yields a New Class of Inhibitors of HGF/SF-MET Binding. *Chem. Sci.* **2015**, *6* (11), 6147–6157.
- (51) Blanco, F. F.; Preet, R.; Aguado, A.; Vishwakarma, V.; Stevens, L. E.; Vyas, A.; Padhye, S.; Xu, L.; Weir, S. J.; Anant, S.; Meisner-

Kober, N.; Brody, J. R.; Dixon, D. A. Impact of HuR Inhibition by the Small Molecule MS-444 on Colorectal Cancer Cell Tumorigenesis. *Oncotarget* **2016**, *7* (45), 74043–74058.

(52) Lang, M.; Berry, D.; Passecker, K.; Mesteri, I.; Bhujji, S.; Ebner, F.; Sedlyarov, V.; Evstatiev, R.; Dammann, K.; Loy, A.; Kuzyk, O.; Kovarik, P.; Khare, V.; Beibel, M.; Roma, G.; Meisner-kober, N.; Gasche, C. HuR Small-Molecule Inhibitor Elicits Differential Effects in Adenomatosis Polyposis and Colorectal Carcinogenesis. *Cancer Res.* **2017**, *77* (9), 2424–2438.

(53) Zhang, Y.; Jiang, P.; Ye, M.; Kim, S. H.; Jiang, C.; Lü, J. Tanshinones: Sources, Pharmacokinetics and Anti-Cancer Activities. *Int. J. Mol. Sci.* **2012**, *13* (10), 13621–13666.

(54) Bocchi, V.; Palla, G. High Yield Selective Bromination and Iodination of Indoles in N,N -Dimethylformamide. *Synthesis* **1982**, *1982* (12), 1096–1097.

(55) Leboho, T. C.; Michael, J. P.; van Otterlo, W. A. L.; van Vuuren, S. F.; de Koning, C. B. The Synthesis of 2- and 3-Aryl Indoles and 1,3,4,5-tetrahydropyrano[4,3-B]indoles and Their Antibacterial and Antifungal Activity. *Bioorg. Med. Chem. Lett.* **2009**, *19* (17), 4948–4951.

(56) Pathak, R.; Nhlapo, J. M.; Govender, S.; Michael, J. P.; van Otterlo, W. A. L.; de Koning, C. B. A Concise Synthesis of Novel Naphtho[a]carbazoles and Benzo[c]carbazoles. *Tetrahedron* **2006**, *62* (12), 2820–2830.

(57) Dong, J.; Feldmann, G.; Huang, J.; Wu, S.; Zhang, N.; Comerford, S. A.; Gayyed, M. F.; Anders, R. A.; Maitra, A.; Pan, D. Elucidation of a Universal Size-Control Mechanism in Drosophila and Mammals. *Cell* **2007**, *130* (6), 1120–1133.

(58) Keene, J. D.; Komisarow, J. M.; Friedersdorf, M. B. RIP-Chip: The Isolation and Identification of mRNAs, microRNAs and Protein Components of Ribonucleoprotein Complexes from Cell Extracts. *Nat. Protoc.* **2006**, *1* (1), 302–307.

(59) Thongon, N.; Castiglioni, I.; Zucal, C.; Latorre, E.; D'Agostino, V.; Bauer, I.; Pancher, M.; Ballestrero, A.; Feldmann, G.; Nencioni, A.; Provenzani, A. The GSK3 β Inhibitor BIS I Reverts YAP-Dependent EMT Signature in PDAC Cell Lines by Decreasing SMADs Expression Level. *Oncotarget* **2016**, *7* (18), 26551–26566.

(60) *Glide*, Schrödinger, LLC: New York, 2014.

(61) Morris, G. M.; Huey, R.; Lindstrom, W.; Sanner, M. F.; Belew, R. K.; Goodsell, D. S.; Olson, A. J. AutoDock4 and AutoDockTools4: Automated Docking with Selective Receptor Flexibility. *J. Comput. Chem.* **2009**, *30* (16), 2785–2791.

(62) *Maestro 10.0.013*; SQL Maestro Group: New York, 2014.

(63) Phillips, J. C.; Braun, R.; Wang, W.; Gumbart, J.; Tajkhorshid, E.; Villa, E.; Chipot, C.; Skeel, R. D.; Kalé, L.; Schulten, K. Scalable Molecular Dynamics with NAMD. *J. Comput. Chem.* **2005**, *26* (16), 1781–1802.

(64) Cornell, W. D.; Cieplak, P.; Bayly, C. I.; Gould, I. R.; Merz, K. M.; Ferguson, D. M.; Spellmeyer, D. C.; Fox, T.; Caldwell, J. W.; Kollman, P. A. A Second Generation Force Field for the Simulation of Proteins, Nucleic Acids, and Organic Molecules. *J. Am. Chem. Soc.* **1995**, *117* (19), 5179–5197.

(65) Lindorff-Larsen, K.; Piana, S.; Palmo, K.; Maragakis, P.; Klepeis, J. L.; Dror, R. O.; Shaw, D. E. Improved Side-Chain Torsion Potentials for the Amber ff99SB Protein Force Field. *Proteins: Struct., Funct., Genet.* **2010**, *78* (8), 1950–1958.

(66) Allnér, O.; Nilsson, L.; Villa, A. Magnesium Ion–Water Coordination and Exchange in Biomolecular Simulations. *J. Chem. Theory Comput.* **2012**, *8* (4), 1493–1502.

(67) Bayly, C. I.; Cieplak, P.; Cornell, W.; Kollman, P. A. A Well-Behaved Electrostatic Potential Based Method Using Charge Restraints for Deriving Atomic Charges: The RESP Model. *J. Phys. Chem.* **1993**, *97* (40), 10269–10280.

(68) Frisch, M. J.; Trucks, G. W.; Schlegel, H. B.; Scuseria, G. E.; Robb, M. A.; Cheeseman, J. R.; Scalmani, G.; Barone, V.; Mennucci, B.; Petersson, G. A.; Nakatsuji, H.; Caricato, M.; Li, X.; Hratchian, H. P.; Izmaylov, A. F.; Bloino, J.; Zheng, G.; Sonnenberg, J. L.; Hada, M.; Ehara, M.; Toyota, K.; Fukuda, R.; Hasegawa, J.; Ishida, M.; Nakajima, T.; Honda, Y.; Kitao, O.; Nakai, H.; Vreven, T.; Montgomery, J. A., Jr;

Peralta, J. E.; Ogliaro, F.; Bearpark, M.; Heyd, J. J.; Brothers, E.; Kudin, K. N.; Staroverov, V. N.; Kobayashi, R.; Normand, J.; Raghavachari, K.; Rendell, A.; Burant, J. C.; Iyengar, S. S.; Tomasi, J.; Cossi, M.; Rega, N.; Millam, J. M.; Klene, M.; Knox, J. E.; Cross, J. B.; Bakken, V.; Adamo, C.; Jaramillo, J.; Gomperts, R.; Stratmann, R. E.; Yazyev, O.; Austin, A. J.; Cammi, R.; Pomelli, C.; Ochterski, J. W.; Martin, R. L.; Morokuma, K.; Zakrzewski, V. G.; Voth, G. A.; Salvador, P.; Dannenberg, J. J.; Dapprich, S.; Daniels, A. D.; Farkas, O.; Foresman, J. B.; Ortiz, J. V.; Cioslowski, J.; Fox, D. J. *Gaussian 09*, Revision B.01; Gaussian, Inc.: Wallingford, CT, 2009.

(69) Dupradeau, F.-Y.; Pigache, A.; Zaffran, T.; Savineau, C.; Lelong, R.; Grivel, N.; Lelong, D.; Rosanski, W.; Cieplak, P. The R.E.D. Tools: Advances in RESP and ESP Charge Derivation and Force Field Library Building. *Phys. Chem. Chem. Phys.* **2010**, *12* (28), 7821–7839.

(70) Vanqualef, E.; Simon, S.; Marquant, G.; Garcia, E.; Klimerak, G.; Delepine, J. C.; Cieplak, P.; Dupradeau, F.-Y. R.E.D. Server: A Web Service for Deriving RESP and ESP Charges and Building Force Field Libraries for New Molecules and Molecular Fragments. *Nucleic Acids Res.* **2011**, *39* (Web Server issue), W511–W517.

(71) Wang, J.; Wang, W.; Kollman, P. A.; Case, D. A. Automatic Atom Type and Bond Type Perception in Molecular Mechanical Calculations. *J. Mol. Graphics Modell.* **2006**, *25* (2), 247–260.

(72) Humphrey, W.; Dalke, A.; Schulten, K. VMD: Visual Molecular Dynamics. *J. Mol. Graphics* **1996**, *14* (1), 33–38 pp 27–28.

(73) Roe, D. R.; Cheatham, T. E. PTRAJ and CPPTRAJ: Software for Processing and Analysis of Molecular Dynamics Trajectory Data. *J. Chem. Theory Comput.* **2013**, *9* (7), 3084–3095.

(74) Michaud-Agrawal, N.; Denning, E. J.; Woolf, T. B.; Beckstein, O. MDAnalysis: A Toolkit for the Analysis of Molecular Dynamics Simulations. *J. Comput. Chem.* **2011**, *32* (10), 2319–2327.

(75) Pettersen, E. F.; Goddard, T. D.; Huang, C. C.; Couch, G. S.; Greenblatt, D. M.; Meng, E. C.; Ferrin, T. E. UCSF Chimera—a Visualization System for Exploratory Research and Analysis. *J. Comput. Chem.* **2004**, *25* (13), 1605–1612.

(76) Hunter, J. D. et al. *Matplotlib v2.0.2*; Matplotlib Development Team, 2017.